

Accepted Manuscript

Modelling scale-dependent runoff generation in a small semi-arid watershed accounting for rainfall intensity and water depth

Christoph Langhans, Gerard Govers, Jan Diels, Jeffrey J. Stone, Mark A. Nearing

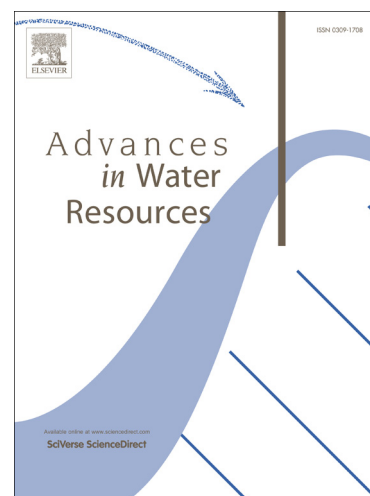
PII: S0309-1708(14)00056-6
DOI: <http://dx.doi.org/10.1016/j.advwatres.2014.03.005>
Reference: ADWR 2176

To appear in: *Advances in Water Resources*

Received Date: 19 October 2012
Revised Date: 31 January 2014
Accepted Date: 24 March 2014

Please cite this article as: Langhans, C., Govers, G., Diels, J., Stone, J.J., Nearing, M.A., Modelling scale-dependent runoff generation in a small semi-arid watershed accounting for rainfall intensity and water depth, *Advances in Water Resources* (2014), doi: <http://dx.doi.org/10.1016/j.advwatres.2014.03.005>

This is a PDF file of an unedited manuscript that has been accepted for publication. As a service to our customers we are providing this early version of the manuscript. The manuscript will undergo copyediting, typesetting, and review of the resulting proof before it is published in its final form. Please note that during the production process errors may be discovered which could affect the content, and all legal disclaimers that apply to the journal pertain.



1
2 1 Title: Modelling scale-dependent runoff generation in a small semi-arid
3
4
5 2 watershed accounting for rainfall intensity and water depth
6
7
8

9
10 3 Corresponding Author: Christoph Langhans^{1,2}
11

12 4 Co-Author: Gerard Govers¹
13

14 5 Co-Author: Jan Diels¹
15

16 6 Co-Author: Jeffry J. Stone³
17

18 7 Co-Author: Mark A. Nearing³
19
20
21

22
23 8 Affiliations:
24

25
26 9 ¹ Department of Earth and Environmental Sciences, KULeuven, Celestijnenlaan 200 E,
27
28 10 3001 Heverlee, Belgium
29

30
31 11 ²Currently at: Forest and Water Group, Department of Forest and Ecosystem Science,
32
33 12 Melbourne School of Land and Environment, University of Melbourne, 221 Bouverie St,
34
35 13 3010 Parkville, Victoria, Australia
36

37
38 14 ³ Southwest Watershed Research Center, USDA-ARS, 2000 E. Allen Rd, 85719 Tucson,
39
40 15 AZ, USA
41
42

43
44 16
45
46
47
48
49
50
51
52
53
54
55
56
57
58
59
60
61
62
63
64
65

Abstract:

Observed scale effects of runoff on hillslopes and small watersheds derive from complex interactions of time-varying rainfall rates with runoff, infiltration and macro- and microtopographic structures. A little studied aspect of scale effects is the concept of water depth-dependent infiltration. For semi-arid rangeland it has been demonstrated that mounds underneath shrubs have a high infiltrability and lower lying compacted or stony inter-shrub areas have a lower infiltrability. It is hypothesized that runoff accumulation further downslope leads to increased water depth, inundating high infiltrability areas, which increases the area-averaged infiltration rate. A model was developed that combines the concepts of water depth-dependent infiltration, partial contributing area under variable rainfall intensity, and the Green-Ampt theory for point-scale infiltration. The model was applied to rainfall simulation data and natural rainfall – runoff data from a small sub-watershed (0.4 ha) of the Walnut Gulch Experimental Watershed in the semi-arid US Southwest. Its performance to reproduce observed hydrographs was compared to that of a conventional Green-Ampt model assuming complete inundation sheet flow, with runoff infiltration, which is infiltration of runoff onto pervious downstream areas. Parameters were derived from rainfall simulations and from watershed-scale calibration directly from the rainfall – runoff events. The performance of the water depth-dependent model was better than that of the conventional model on the scale of a rainfall simulator plot, but on the scale of a small watershed the performance of both model types was similar. We believe that the proposed model contributes to a less scale-dependent way of modelling runoff and erosion on the hillslope-scale.

Keywords:

Runoff, runoff, infiltration, Green-Ampt, Walnut Gulch, modelling, water depth

1 Introduction

The scale-dependency of runoff and infiltration has been recognized widely. In studies that compare runoff at different scales of a hillslope, scale effects appear as reduced runoff coefficients with increasing scale [1-7]. Models that try to reduce scale-dependency in the calculation of runoff generation have concentrated on various effects. Among the explanations for scale effects, variability and duration of a rainstorm are probably the most uncontroversial ones: even on a perfectly homogeneous surface runoff coefficients can be expected to decrease with slope length (or area) due to the infiltration of runoff water in pervious downstream areas (runon infiltration) during periods of low rainfall intensity and/or after the rainfall event. Stomph et al. [8] have quantified the effect of storm duration and slope length on artificial slopes in the laboratory, finding that shorter rainfall durations and longer slopes produce the largest scale effects. Wainwright and Parsons [9] simulated runoff coefficients with a simple storage model, allowing runon infiltration, which is defined as infiltration of water produced by rainfall excess further upslope [10]. They found that the average rainfall intensity and variability of rainfall strongly influenced runoff coefficients, while the reduction in runoff coefficients with slope length of the simulated hillslope was dependent on slope gradient and the hydraulic roughness coefficient. The effect of spatial variation in infiltration capacity on scale effects is more controversial than the temporal effect. Modelling studies have created randomly distributed hydraulic variables, very often saturated hydraulic conductivities (K_s), with or without spatial correlation, and have computed the sensitivity of runoff production to the coefficient of variance and/or the spatial structure of the variance [10-12]. If runon infiltration is allowed, which means that runoff produced upstream infiltrates if it flows over unsaturated areas, substantial scale effects appear [13-15].

64 It has been suggested that heterogeneity in the context of runoff infiltration increases scale
65 effects, because the likelihood that runoff flows onto areas of very high infiltration capacity is
66 increased with increasing scale, thereby reducing runoff connectivity [7, 16]. However, the
67 effect is dependent on rainfall intensity and duration, the pattern of runoff concentration and
68 typical scale of heterogeneities [17], and it has not been quantified yet.

69 Runon infiltration is usually modelled as sheet flow entering unsaturated modelling units
70 (cells or pixels), supplying water for infiltration in the same way as rainfall on the whole
71 surface of the modelling unit [e.g. 13]. In such a conceptualization a constant hydraulic
72 conductivity for the whole modelling unit is assumed. Runon infiltration has also been
73 modelled to increase with inundation of a microtopography, albeit without a systematic
74 variation of hydraulic conductivity within the microtopography [10]. However, in
75 environments with a clear microtopographical pattern, the local distribution of hydraulic
76 conductivities is not completely random nor constant, but dependent on the relative elevation
77 within the microtopography. Lyford and Qashu [18] found hydraulic conductivities to be 2.6
78 times higher under creosote bushes (*Larrea tridentata*) and Palo Verde (*Cercidium*
79 *microphyllum*), compared to the lower lying inter-shrub area. Similarly, Johnson and Gordon
80 [19] have found 2 – 2.5 times higher infiltration rates under sagebrush (*Artemisia tridentata*)
81 as compared to the inter-shrub areas. For the Mediterranean semi-arid rangeland
82 environments it has been described how increased infiltration rates occur closer to plants as a
83 consequence of mound build-up and improvement of the physical and chemical soil properties
84 around the plant [e.g. 20, 21]. Dunne et al. [22] have proposed a model for steady state
85 infiltration that accounts for these systematic patterns. In their model infiltration per unit area
86 increased with increasing runoff water depth towards the foot of a slope. This increase is
87 achieved by inundation of parts of an elevation-dependent distribution of hydraulic
88 conductivities, where higher conductivities are associated with higher elevation of the

89 microtopography. The typical distance between mounded plants may influence runoff
90 thresholds and scale effects [23]. Dunne et al. [22] combined the concept of water depth-
91 dependent infiltration with the concept of partial contributing area for runoff production in
92 order to explain the convex shape of shrub-covered hillslopes in Kenya. However, they did
93 not account for temporal variations in rainfall intensity and/or infiltration capacity. Also in
94 agricultural environments the spatial variation in infiltration capacity shows clear structure,
95 leading to water depth dependent infiltration rates. Bresson and Valentin [24] showed that on
96 tilled fields a sedimentary crust with a low hydraulic conductivity builds up in the micro-
97 valleys while the micro-slopes and ridges are covered by a structural crust with much higher
98 conductivity. Fox et al. [25] have subsequently shown in a laboratory study that this
99 phenomenon can lead to a fourfold increase in average hydraulic conductivity with increasing
100 water depth. Langhans et al. [26-28] have shown that under varying inflow and rainfall
101 intensity rates on small rainfall simulation plots infiltration rates increase as inflow, rainfall
102 intensity, water depth and inundated area increase. They have accounted for these effects in a
103 water-depth dependent infiltration model based on Green-Ampt [27]. Clearly, if runoff
104 infiltration is water depth-dependent this may produce scale effects as, generally, water depths
105 can be expected to increase with increasing contributing area. While both temporal variation
106 in rainfall (and infiltration) and the depth-dependency of infiltration may cause scale effects, a
107 modelling framework integrating both effects has not yet been empirically tested on both the
108 rainfall simulation plot-scale and the hillslope or small catchment-scale under natural rainfall
109 conditions.

110 The model first described in Langhans et al. [27] for a steady state case, integrates
111 temporal, water depth and rainfall intensity effects and enables the exploration of the relative
112 importance of these effects on scale effects. In the present study, behaviour and performance
113 are compared to a similar baseline model without water depth-dependency and with a sheet

114 flow assumption. Data for testing the models were rainfall simulations on plots, and small
115 catchment runoff measurements, constituting two typical scales where we would expect
116 runoff generation rates to decrease from plot- to catchments-scale. We chose to form
117 infiltration expressions with parameters that are effective at the local scale (resolution) of
118 approximately 1 m² [29]. The actual resolution of a model unit in a distributed model should
119 be similar to the typical scale length of microtopography to be able to capture the full process
120 of interaction between runoff and microtopography. The typical scale length therefore
121 depends on land use: in agricultural systems, tillage implements determine the width of the
122 microtopography (~0.3 m), while in semi-arid rangeland of the study area shrubs on mounds
123 are organized in intervals of ~1.5 m. An advantage of conceptualizing processes at the local
124 scale is that effective parameters can be readily found by parameterizing the model with
125 rainfall simulation data, because the scale of modelling units and experimental plots are
126 similar and it can be assumed that processes within the experimental plot resemble those of
127 the modelling unit.

128 In this study we seek to answer the following questions: (1) can we observe scale effects
129 in a data set of rainfall simulations and runoff data from small catchments? (2) Can both
130 watershed-scale infiltration models be successfully calibrated using rainfall simulation data or
131 is calibration from watershed-scale runoff data necessary? (3) Does the incorporation of the
132 water depth-dependency and runoff infiltration into a Green-Ampt based model improve
133 performance?

134

135 2 Methods

1
2
3
4 136 This section describes the site and the rainfall simulation data that were used to parameterize
5
6 137 the baseline model and the new model to be tested. Further, this section describes the natural
7
8 138 rainfall data that were used to validate the models' results when parameterized with rainfall
9
10
11 139 simulation data and to obtain model parameters by calibration and validation against runoff
12
13 140 hydrographs. The parameterization is described in detail in section 3.4.
14
15
16

17 2.1 Site description

18
19
20 142 The Walnut Gulch Experimental Watershed (WGEW) of the United States Department of
21
22 143 Agriculture (USDA) is a semi-arid watershed located in Southeast Arizona, southwest United
23
24
25 144 States in the transition zone between the Sonoran and Chihuahuah desert (Figure 1). Runoff
26
27 145 occurs mainly in the summer months during and shortly after major convective storms.
28
29
30 146 Storms of lower intensity during winter months rarely produce runoff. Within the WGEW, the
31
32 147 Lucky Hills Site is a 0.4 ha sub-watershed (LH- 106) with an average slope of 7.6 %, and
33
34
35 148 equipped with an H-flume [30]. Figure 2 is a contour map of the watershed, under-laid with a
36
37 149 panchromatic satellite image from 7 July 2010 (Quickbird, 0.6 m resolution). The darker gray
38
39
40 150 areas represent single shrubs or agglomerations of a few shrubs (1 to 2 m in diameter), within
41
42 151 a network of gravelly soil or scattered forbs and grasses, mostly with a stony upper soil layer
43
44
45 152 (light grey areas). The soil is classified as very gravelly sandy loam without a topsoil [31].
46
47 153 Dominant shrubs species within the watershed include Creosote (*Larrea tridentata*) and
48
49 154 Whitethorn (*Acacia constricta*) on mounds of looser, mulched soil with fewer stones (Figure
50
51
52 155 3).
53

54 156

57 157 [location of Figure 1, 2 and 3]
58
59
60
61
62
63
64
65

158

2.2 Rainfall simulations and runoff measurements

Rainfall simulations with rainfall intensities between 25 and 216 mm h⁻¹ were conducted between 2004 and 2008 during summer months about 100 meters south of the outlet of LH-106. Rainfall simulations were conducted with a central oscillating boom rainfall simulator with four nozzles (Veejet 80100) attached at 1.52 m intervals, mounted 3 m above ground, while the plot was protected with a wind shield [32]. Details on the experimental procedure are given in Stone et al. [33]. A dry run at initial soil moisture was followed 45 minutes later by a wet or very wet run. The experiments chosen as the calibration set were wet and very wet runs from 2007 and 2008 on 6 large plots (LP) of 6.1 by 2 m, with apparent steady state runoff reached after application of at least 5 minutes of rainfall. These experiments were chosen as the calibration set, because orthogonal photos of the plot during experiments and dye velocity measurements (u , LT⁻¹) existed for them which were required for the parameterization of the model (Table 1). The photos covered the lower 3 m of the runoff plot, and on three transects along the plot width, w_p (L), at lengths of approximately 3.75, 4.5 and 5.25 m from the upper plot border, the width fraction of inundation was measured by visual interpretation. Usually, it could easily be seen which parts were covered by water or not, however, stone pavements protruding through a layer of water occasionally created uncertainty in the visual interpretation. Runoff alternated between more concentrated faster flow around vegetated mounds and broader sheetflow in between. Water often flowed along the lateral plot borders. A trend towards more inundation at the lower end of the plot was not present. Consequently, all three transect measurements were averaged to form a single inundated area fraction (A_i), representative for the plot. Mean flow velocity was computed using the centroid of the electrical resistivity curve measured at the outlet of the plot [34].

182 Rainfall simulations on large plots from 2004 (four plots), where no photos were taken, and
183 small plots (SP, 0.75 m², 3 plots) from 2008, were used as validation (Table 1).

184 Natural rainfall – runoff events were selected from a continuous period of runoff and
185 rainfall measurements from 2001 to 2010. Rainfall depth was digitally recorded at 1 min
186 increments during periods of rainfall at a gage about 100 m from the outlet of LH-106. The
187 runoff hydrograph was measured also as breakpoint data at the H-Flume (Figure 2). During
188 this period 718 rainfall events were recorded of which 60 resulted in runoff. All runoff events
189 except for one (23.07.2008) had incident rainfall totals of more than 4.5 mm. Thus, this value
190 was chosen as a minimum threshold for the selection of a dataset of rainfall events to be
191 analysed. Volumetric soil moisture content at 5 cm depth was measured at a meteorological
192 station 270 meters north of LH-106. The maximum value was taken as the effective saturated
193 soil moisture content or effective porosity, η_e (L³L⁻³) = 0.29. To obtain a relevant estimate of
194 initial soil moisture content, θ_i (L³L⁻³) a value just before rainfall started was selected for each
195 event. Five rainfall events, of which one was producing runoff (07.07.2001), had no soil
196 moisture measurements. The deletion of these events and the use of the rainfall threshold
197 resulted in a total of 147 rainfall events with 58 producing runoff (Table 1). Selecting rainfall
198 events with a threshold rather than selecting only runoff events reflects the fact that in a
199 rainfall – runoff model rainfall is an independent variable while runoff is the quantity to be
200 predicted.

201
202 [location of Table 1]

203 3 Model descriptions

204 Two contrasting models for the calculation of infiltration and runoff hydraulics at the
 205 local scale of a modelling unit are presented. Both were applied in a distributed model for the
 206 calculation of runoff at the small watershed-scale.

208 3.1 Conventional Green-Ampt model with sheet flow (CON)

209 The model to which the new proposed model is compared is termed conventional,
 210 because it uses equations that are commonly used to model runoff on hillslopes. Infiltrability
 211 (f_t) at the point-scale, assuming piston-type flow is given by the Green-Ampt Equation [35]
 212 [e.g. Equation 5.4.1 in 36]:

$$214 \quad f_t = K_s \left(\frac{\psi \Delta \theta}{F_t} + 1 \right) \quad (1)$$

215 where K_s is the point-scale hydraulic conductivity (LT^{-1}), ψ (L) is the suction across the
 216 wetting front and $\Delta \theta$ (L^3L^{-3}) is the difference between η_e and θ_i . F_t is the cumulative
 217 infiltration at the end of a time step, which is given by Equation 5.4.2 in Chow et al. [36]:

$$219 \quad F_t = F_{t-\Delta t} + K_s \Delta t + \psi \Delta \theta \ln \left(\frac{F_t + \psi \Delta \theta}{F_{t-\Delta t} + \psi \Delta \theta} \right) \quad (2)$$

221 The use of Equations 1 and 2 for the application to variable intensity rainstorms has been
 222 described by Chu [37]. Under the assumption of zero heterogeneity, point-scale K_s equals the

224 effective hydraulic conductivity K_e (LT^{-1}). When the surface becomes saturated at ponding
 1
 2 225 time, infiltration is assumed to occur below a thin continuous water layer covering the whole
 3
 4 226 modelling unit. Equally, runoff that enters a modelling unit is effectively distributed over the
 5
 6
 7 227 whole surface area and is added to rainfall to form a common water influx.

8
 9 228 For modelling runoff on a hillslope, a roughness coefficient is required for the estimation
 10
 11
 12 229 of flow depth. We chose to use Manning's n , as it can be assumed that flow either becomes
 13
 14 230 turbulent as it concentrates downslope, or it is laminar or intermediate, but much disturbed by
 15
 16
 17 231 roughness elements such as stones or litter. The average flow depth D (L) of the whole
 18
 19 232 modelling unit is calculated as:

$$20
21
22 233
23
24
25
26 234 \quad D = \left(\frac{n}{S^{1/2}} q_e \right)^m \quad (3)$$

27
28
29 235
30
31
32 236 where q_e (L^2T^{-1}) is the effective or average unit width discharge of a modelling unit, S is
 33
 34 237 the gradient of the water surface, assumed to be equal to the slope gradient, and m is an
 35
 36
 37 238 exponent which is 0.6 for turbulent flow [38].

38
 39 239 At its core, the CON model contains Chu's variable rainfall intensity Green and Ampt
 40
 41
 42 240 infiltration model [37], with the main addition of the possibility of runoff infiltration (r_{in})

43
 44 241 (Figure 4)

45
 46 242
 47
 48
 49 243 [location of Figure 4]

50
 51 244
 52
 53
 54
 55
 56
 57
 58
 59
 60
 61
 62
 63
 64
 65

245 3.2 Water depth-dependent Green-Ampt model with partial inundation

1
2
3 246 (WDD)
4

5
6 247 Contrary to the sheetflow assumption, the WDD model acknowledges that there is
7
8 248 microtopography. This means that for every level of inundation within the microtopography,
9
10 249 there is an average water depth positively correlated to the inundation fraction A_i . The type of
11
12 250 this relationship will depend on the microtopography. As a first approximation we used a
13
14 251 linear relationship between the inundation fraction and water depth.
15
16
17

18 252
19
20
21 253
$$A_i = bD \tag{4}$$

22
23

24 254

25
26 255 with b an empirical constant. Equation 4 does not imply that there is a single channel per
27
28 256 modelling unit; it is purely empirical and can contain any amount of micro-channels that can
29
30 257 take a tortuous route. These surface and flow characteristics (e.g. flow through protruding
31
32 258 stones in this study) are accounted for by Manning's n . As there are inundated and not
33
34 259 inundated areas, q_e in Equation 3 should apply for the inundated area only. The average
35
36 260 effective plot unit runoff r_e (LT^{-1}) is computed by averaging the inflow r_{in} (LT^{-1}) from upslope
37
38 261 area and the outflow r_{out} (LT^{-1}) from a modelling unit:
39
40
41
42

43 262
44
45
46 263
$$r_e = (r_{in} + r_{out}) / 2 \tag{5}$$

47
48

49 264

50
51 265 Unit width discharge in the WDD model is for width of the inundated area only, so it is
52
53 266 defined in relation to r_e as:
54
55

56 267

$$q_e = l_p r_e A_i^{-1} \quad (6)$$

where l_p (L) is the length of the modelling unit. The depth-discharge relationship can now be adapted for the WDD model, by substituting Equation 4 into Equation 6, which was then substituted into Equation 3:

$$D = \left(\frac{n l_p r_e}{S^{1/2} b} \right)^{\frac{m}{1+m}} \quad (7)$$

Hydraulic conductivities in the WDD model are assumed to have an exponential distribution, an assumption that has been successfully tested elsewhere [33, 39, 40]:

$$g(K_s) = \frac{1}{\mu_K} \exp\left(-\frac{K_s}{\mu_K}\right) \quad (8)$$

where $g(K_s)$ is the probability distribution of hydraulic conductivities on the scale of the microtopography, within a modelling unit, with μ_K (LT^{-1}) their mean, which is assumed constant. We did not assume a random distribution but one that is monotonically increasing with relative elevation of the microtopography, which is in line with field observations (see introduction). This assumption has been made before, but not in conjunction with the exponential distribution [22, 25]. Hawkins [39] formalized the partial contributing area approach: at any rainfall intensity (i , LT^{-1}), there is always some area where rainfall intensity is limiting infiltration and some area where the soil's infiltration capacity is limiting infiltration, the latter termed runoff contributing area fraction (A_c). In the small-scale context

290 of the microtopography, A_c can be interpreted as the area where water flows erratically,
 291 depending on actual raindrop impact towards an inundated area (Figure 5a). When rainfall
 292 starts, A_c is infinitely small, but once soil suction decreases and rainfall intensity increases, a
 293 substantial area fraction can contribute to runoff production (Figure 5a). When water
 294 accumulates and concentrates further downstream, or when there is a sudden decrease in
 295 rainfall intensity during or at the end of a storm, the accumulated water can inundate an area
 296 bigger than A_c (Figure 5b). In this case runoff infiltration will occur on the inundated area.
 297 Figure 5a and b depict a single channel for clarity of the illustration, but the generalized
 298 model (Equation 4) does not require a specific microtopography form.

[location of Figure 5a and 5b]

In the case of an exponential distribution with a single mean parameter, and when ψ and $\Delta\theta$ are spatially constant, the mean infiltration capacity μ_f (LT^{-1}) is proportional to μ_K , just like f_i is proportional to K_s (Equation 1) on the point-scale:

$$\mu_f = \mu_K \left(\frac{\psi \Delta\theta}{F_t} + 1 \right) \quad (9)$$

Equation 9 assumes that there is sufficient horizontal redistribution of infiltrated water to form a single infiltration front. It has been shown that an average Green-Ampt infiltration front produced results close to a three-dimensional finite difference solution [41]. F_t , the cumulative infiltration of the time step is not known when it is required in Equation 9, so the cumulative infiltration of the previous time step $F_{t-\Delta t}$ (with Δt being the time interval) is used

313 as an initial guess (Figure 6). During subsequent iterations within the time step the value of F_t
 1
 2 314 is updated.

3
 4 315
 5
 6
 7 316 [location of Figure 6]

8
 9 317
 10
 11
 12 318 Equation 9 yields μ_f which is necessary for the calculation of A_c . As A_c is defined as the
 13
 14 319 area fraction where the infiltration capacity is less than the rainfall intensity i , it is obtained by
 15
 16
 17 320 integrating the exponential distribution of infiltration capacities $g(f)$ from 0 to i which yields:

18
 19 321
 20
 21
 22
 23 322
$$A_c = \int_0^i g(f)df = 1 - \exp\left(-\frac{i}{\mu_f}\right) \quad (10)$$

24
 25
 26
 27 323
 28
 29 324 where $g(f)$ is the same as $g(K_s)$ in Equation 8, only that μ_K is substituted with μ_f . Like A_c , A_i is
 30
 31
 32 325 also a function of the exponential distribution:

33
 34 326
 35
 36
 37
 38 327
$$A_i = \int_0^{K_s(A_i)} g(K_s)dK_s = 1 - \exp\left(-\frac{K_s(A_i)}{\mu_K}\right) \quad (11)$$

39
 40
 41
 42 328
 43
 44 329 where $K_s(A_i)$ is the hydraulic conductivity at the edge of the water level of inundation.
 45
 46
 47 330 Similarly, $K_s(A_c)$ is the hydraulic conductivity at the edge of the runoff contributing area.

48
 49 331
 50
 51
 52 332
$$K_s(A_{c|i}) = -\ln(1 - A_{c|i})\mu_K \quad (12)$$

53
 54
 55 333

334 Where $A_{c|i}$ is either A_c or A_i . The average hydraulic conductivity of the runoff
 335 contributing area K_c and the average hydraulic conductivity of the inundated are K_i are
 336 obtained by integrating hydraulic conductivities from the exponential distribution $g(K_s)$ from
 337 0 to $K_s(A_{c|i})$, which yields:

$$338 \quad K_{c|i} = \int_0^{K_s(A_{c|i})} K_s g(K_s) dK_s = \mu_K - (1 - A_{c|i}) (\mu_K + K_s(A_{c|i})), \quad (13)$$

340
 341 Where $K_{c|i}$ is either K_c or K_i . F_t can now be calculated as:

$$342 \quad F_t = F_{t-\Delta t} + i\Delta t(1 - A_{c|i}) + A_{c|i} \left(K_{c|i} \Delta t + \psi \Delta \theta \ln \left(\frac{F_t + \psi \Delta \theta}{F_{t-\Delta t} + \psi \Delta \theta} \right) \right) \quad (14)$$

344
 345 with $A_{c|i} = A_i$ and $K_{c|i} = K_i$ if $A_i > A_c$ (case Figure 5b), and else $A_{c|i} = A_c$ and $K_{c|i} = K_c$ (case
 346 Figure 5a). Equation 14 is derived from Equation 2, splitting the cumulative infiltration into a
 347 part where rainfall infiltrates directly (the second term) and a part where infiltration during a
 348 time step under A_i or A_c is limited by the soil (the third term). The resulting value of F_t is still
 349 an approximation and the calculation of Equations 9 to 14 are repeated until F_t used in
 350 Equation 9 differs from the outcome in Equation 15 by less than a very small threshold value.
 351 The effective infiltration rate f_e (LT^{-1}) of the modelling unit is now given by:

$$352 \quad f_e = i(1 - A_{c|i}) + K_{c|i} \left(\frac{\psi \Delta \theta}{F_t} + 1 \right) A_{c|i}. \quad (15)$$

355 The first term is infiltration equal to rainfall intensity on the non-inundated and no runoff
1
2 356 producing part of the soil and the second term describes infiltration according to the Green-
3
4 357 Ampt equation on the remaining inundated or runoff producing area.
5
6

7 358

10 359 3.3 2D distributed Model

11
12
13
14 360 Both infiltration models are implemented in MCST [47], a spatially distributed runoff-erosion
15
16 361 model that originally used a modified curve number approach. The model routes runoff using
17
18
19 362 the kinematic wave equation in conjunction with a flux decomposition algorithm [43] [48].
20

21 363 A digital elevation model of the watershed with a 1 m horizontal resolution from a RTK
22
23 364 GPS survey with 426 elevation points was used [42]. Infiltration and runoff calculation was
24
25
26 365 changed so that runoff infiltration could be accounted for in each grid cell and at each time
27
28
29 366 step. Following the logic of the linear scheme of the kinematic wave algorithm, r_e in Equation
30
31 367 5 was calculated with r_{in} as inflow into a modelling unit during the present time step and r_{out}
32
33 368 as the outflow calculated on the same modelling unit during the previous time step. In the
34
35
36 369 CON model the estimate of r_e was added to the rainfall intensity to calculate the amount of
37
38 370 water which was available for infiltration on the whole surface of the modelling unit in
39
40
41 371 accordance with the sheet flow assumption. In the WDD model, r_e was used to calculate D
42
43 372 (Equation 7) and A_i (Equation 4) and then infiltration as described above. For a given set of
44
45
46 373 parameter values controlling infiltration the WDD model will always predict lower runoff
47
48 374 infiltration for the same runoff amount, unless there is full inundation. Once infiltration is
49
50
51 375 calculated in both models, an estimate for the net lateral inflow into a modelling unit during a
52
53 376 time step, Δr (LT^{-1}), is obtained, which can become negative during runoff infiltration, and is
54
55 377 given by the difference between rainfall intensity and infiltration. It relates to the kinematic
56
57
58 378 wave equation as:

379

$$\frac{\partial(r_{out}l_p)}{\partial l_p} + \frac{\partial D}{\partial t} = \Delta r = i - f_e \quad (16)$$

381

Equation 17 was solved using a discrete non-linear scheme [36]. So for each time step and modelling unit, runoff, infiltration, water depth, and in the case of the WDD model, inundated area fraction are estimated. For a single rainfall event, three main output quantities were calculated that could be compared to measured quantities: the total discharge, Q_t (L^3), which is the sum of discharge of all time steps at the modelling unit (cell) that represents the outlet of the watershed. The steady state effective discharge, Q_e (L^3T^{-1}), is a quantity that is used in erosion modelling, also in the MCST model, and is given by [43]:

389

$$Q_e = \left(\frac{\sum_{t=t_1}^{t_n} Q^{1.4}}{\sum_{t=t_1}^{t_n} Q} \right)^{2.5} \quad (17)$$

391

where Q (L^3T^{-1}) is the discharge during one time step t , with t_1 the first and t_n the last time step of an event. The third quantity is peak discharge, Q_p , (L^3T^{-1}). All three quantities can be modelled and also derived from observational hydrographs, measured at the H-flume at the watershed outlet.

396

397 3.4 Model parameterization and evaluation

1
2
3 398 In accordance with the second objective, the model was parameterized using the
4
5 399 calibration set of rainfall simulations to find values for K_e and μ_K for the CON and the WDD
6
7
8 400 model, respectively, and values of Manning's n and the parameter b , the latter for the WDD
9
10 401 model. Secondly, K_e , μ_K , ψ and n were calibrated for natural rainfall-runoff events by
11
12
13 402 optimizing an objective function consisting of the Nash-Sutcliffe model efficiency (ME) and
14
15 403 the coefficient of determination (R^2) of predictions of Q_t , Q_e and Q_p , where R^2 was defined as:

16
17
18 404
19
20
21
22 405
$$R^2 = ME = 1 - \frac{\sum_{i=1}^n (X_{observed} - X_{predicted})^2}{\sum_{i=1}^n (X_{observed} - X_{mean})^2} \quad (18)$$

23
24
25
26
27 406
28
29
30 407 where X is the quantity of interest. When equation 19 is used to calculate ME, X is the
31
32 408 instantaneous runoff rate during a time step. All parameters were assumed to be constant
33
34 409 within the catchment.
35
36

37 410 38 39 40 411 3.4.1 Parameterization using rainfall simulations

41
42
43 412 An estimate of average plot width flow depth on the rainfall simulation plots (assuming
44
45
46 413 sheet flow) was obtained for the CON model using measured average velocities:
47
48
49 414

50
51
52 415
$$D = \frac{r_e l_p}{u} \quad (19)$$

417 where r_e was calculated from Equation 5 with measured r_{out} and zero r_{in} . This allowed to
 1
 2 418 find a value for Manning's n that minimized the square of the residuals between predicted and
 3
 4
 5 419 measured D , using observed D , r_e and S data (least squares method) (Equation 3).

6
 7 420 For the WDD model, D is defined for the inundated area only, so Equation 20 becomes:
 8

$$D = \frac{r_e l_p}{u A_i} \quad (20)$$

9 421
 10
 11
 12
 13
 14 422
 15
 16
 17 423
 18
 19
 20 424 A_i values were measured as described in section 2.2. D in Equation 21 was substituted
 21
 22 425 with A_i/b (Equation 4) and then b was optimized with the least squares method for predicted
 23
 24
 25 426 and measured r_{out} . Similarly to the CON model, Manning's n could now be found with the
 26
 27 427 least squares method (Equation 7).

28
 29
 30 428 As K_e was assumed to approximately equal measured final infiltration rates during the
 31
 32 429 (wet run) rainfall experiments, for the CON model an estimate of average K_e is simply derived
 33
 34
 35 430 by averaging final infiltration rates of the calibration dataset. For the WDD model, μ_K was
 36
 37 431 optimized as described and depicted in Figure 9, dashed area, in Langhans et al. [27] for the
 38
 39 432 steady state case of the rainfall simulation plots.

434 3.4.2 Calibration on multiple rainfall events

435 The dataset of 147 rainfall events (Table1) was randomly split into a calibration set of 74
 436
 437
 438
 439
 440
 441
 442
 443
 444
 445
 446
 447
 448
 449 435 The dataset of 147 rainfall events (Table1) was randomly split into a calibration set of 74
 450
 451 436 events and a validation set of 73 events. In accordance with objective 3, optimized parameter
 452
 453
 454 437 sets were found for the CON and the WDD model from the calibration set to assess the water
 455
 456 438 depth-dependency effect, and for both models parameter sets were found that assess the effect

439 of runoff infiltration. For the CON model this was done by forcing r_{in} to be zero during
 440 infiltration calculation, and for WDD this was done by forcing A_i to be zero during infiltration
 441 calculation. The objective function (OBJ) was defined as:

$$OBJ = (ME + (R^2(Q_t) + R^2(Q_e) + R^2(Q_p))) / 3) / 2 \quad (21)$$

445 In words, during optimization, the mean R^2 of the predictions of total, effective, and peak
 446 discharge was given equal weight as ME. For CON, ψ , K_e and Manning's n , and for WDD ψ ,
 447 μ_K and Manning's n were simultaneously optimized using the following simple set search
 448 method. Starting values within realistic bounds were chosen, and parameter combinations
 449 were added that were half the starting value's step in each direction of the parameter space
 450 (with three calibration parameters, this results in a 3D grid, when visualized). For each
 451 parameter combination in the set, OBJ was calculated, and the combination with the largest
 452 value was chosen. This combination was used as a new starting point for another set search,
 453 but with half a step size compared to the previous iteration. The number of iteration was
 454 limited by computation time but usually exceeded 4. It was ensured that OBJ were indeed
 455 maximized within the search space by plotting OBJ. The accuracy was between 1-5 mm for
 456 ψ , 0.5 mm/h for K_e and μ_K , and 0.002 for Manning's n .

458 4 Results

459 4.1 Rainfall simulations

460 Water depth of the inundated area show has a clear positive relationship with effective
 461 discharge (WDD, Figure 7), with little scatter for the year 2007. Also, 2007 water depth

462 values are much higher than values of plots from 2008, while the latter level off at 0.002-
1
2 463 0.003 m at high flow rates. The $D - r_e$ relationship under the sheet flow assumption (CON,
3
4 464 Figure 7) shows more scatter and lower depth estimates at higher flow rates, as can be
5
6
7 465 expected, because flow is spread over the whole plot. The relationship of $A_i - r_e$ (not shown)
8
9
10 466 gives the same picture as WDD depths in Figure 7, because A_i and D are related only with the
11
12 467 proportionality parameter b . The range of measured inundation fractions was 0.1 to 0.7.
13
14 468 Values for Manning's n were 0.26 and 0.57 for CON and WDD, respectively.
15
16

17 469
18
19
20 470 [location of Figure 7]
21
22 471
23
24

25 472 Final infiltration rates (K_e) in the years 2007 and 2008 were much higher than they were
26
27 473 in 2004, which were used as validation data (Figure 8). K_e on the small plots in 2008 were
28
29
30 474 more closely in the range of the infiltration values on the long plots. Moreover, K_e showed a
31
32 475 stronger dependency on rainfall intensity in 2007 and 2008 than in 2004. Average K_e , used in
33
34
35 476 the CON model is a constant at 57.2 mm h^{-1} , while μ_K (WDD) was optimized at 62.4 mm h^{-1}
36
37 477 (Table 2). In order to clarify the models' behaviour on the rainfall simulation plot-scale, final
38
39
40 478 infiltration rates were modelled for a range of rainfall intensities for the 6 m plot, with an
41
42 479 average slope of 0.14. The WDD model predicts that the inundation effect (infiltration in area
43
44 480 where A_i exceeds A_c) is strongest around the mean of the distribution on the 6 m plot (solid
45
46
47 481 line departing from dash-dotted line in Figure 8). For the 1 m plots the curve for the average
48
49 482 predicted K_e lies much closer to the curve of the dashed line, because, relatively, less runoff
50
51
52 483 infiltration occurs on a shorter slope (line not shown). Calculated complete inundation at
53
54 484 higher rainfall intensities is a bias produced by the assumption of a linear relationship
55
56
57
58
59
60
61
62
63
64
65

485 between average water depth and inundation. Actually, there are always some parts of the
486 plot, such as mounds under creosote bushes that remain un-inundated.

487
488 [location of Figure 8] [location of Table 2]

489
490 Final infiltration rates on long plots were much lower during 2004 (validation), and both
491 models had negative R^2 . For the small plots (2008), however, the WDD model yielded better
492 predictions ($R^2 = 0.86$) compared to the CON model ($R^2 = 0.10$).

494 4.2 Calibration with rainfall-runoff events

495 Parameter values derived from rainfall simulations were used to model runoff
496 hydrographs of all 147 rainfall events. With hardly any runoff predicted, both models
497 performed poorly, with negative R^2 (Equation 19) (results not shown). Calibration on multiple
498 events at field-scale yielded much lower optimized values for K_e and μ_K , both for model runs
499 with and without runoff infiltration (Table 2). Also, Manning's n values were much smaller
500 than the rainfall experiments suggested. Optimized ψ values were much higher for the WDD
501 than the CON model. The optimization process during calibration yielded clearly defined
502 maxima and smooth contours for OBJ in the parameter space for both models (Figure 9).

503
504 [location of Figure 9 a-d]

505
506 For the calibration set 37% of rainfall-runoff events for both, CON and WDD, had ME
507 values above 0.75 (Table 3). The WDD model however had a higher proportion of events
508 above 0.75 for the validation set. Coefficients of determination for Q_t , Q_p , and Q_e were good

509 for all models and OBJ values were slightly higher for the WDD model than the CON model.

510 The CON model performed slightly better in validation with runon infiltration than without

511 runon infiltration. Comparing observed vs. predicted Q_t revealed that CON had too many

512 events predicting no runoff where there was runoff observed, and, conversely, the WDD

513 model always predicted some runoff, leading to slight overestimation at low runoff rates

514 (figure not shown).

515

516 [location of Table 3]

517

518 4.3 Model behaviour

519 Model behaviour was further studied by comparing predictions of hydrographs with

520 actually observed hydrographs, and by exploring the effects of water depth-dependency and

521 runon infiltration through calculating infiltration under a steady rain (Figure 10). For a 40 mm

522 h^{-1} synthetic rainstorm of 30 minutes, the average watershed-scale infiltration rate for the

523 CON model was equal to rainfall intensity for the first 10 minutes, after which it dropped to

524 below 23 mm h^{-1} at 30 minutes. When allowing runon infiltration, substantial runon

525 infiltration occurred with the CON model between 30 and 40 minutes. For the WDD model

526 infiltration rates dropped immediately after onset of rainfall to below 20 mm h^{-1} at 30

527 minutes. When accounting for runon infiltration, infiltration rates of WDD are only less than

528 0.5 mm h^{-1} larger from minute 8 onwards compared to WDD without runon infiltration, and

529 after 30 minutes runon infiltration drops immediately to 1.5 mm h^{-1} only. Water depth-

530 dependent infiltration under such a scenario is thus negligible, whereas runon infiltration in

531 the CON model is important.

532

533 [location of Figure 10]

534

535 For qualitative analysis of the goodness of hydrograph prediction with the watershed-
536 scale calibration parameters, six events were chosen and displayed: The 90th, 50th, and 10th
537 percentile event, based on descending ranking of ME, both for CON and WDD, with runoff
538 (Figure 11).

539

540 [location of Figure 11]

541

542 For the 90th percentile events, the timing of the peak and peak discharge were better
543 predicted for CON than WDD (Figure 11 a and b). For the 50th percentile events, peak
544 discharge was predicted better with the WDD model (Figure 11, c and d), but timing was
545 either worse (Figure 11 c) or better (Figure 10 d) than CON. For the 10th percentile, WDD had
546 a stronger over estimation of peak discharge than CON (Figure 11 e and f), and timing was
547 not apparently wrong. Regarding the form of the hydrographs, WDD generally has a steeper
548 rise than CON, and follows rainfall intensity more closely. CON hydrographs are usually
549 slightly better timed. Generally, however, over- or under-predictions of total or peak
550 discharge not systematic, except, perhaps a tendency of WDD to over-predict during small
551 events and under-predict during larger events.

552

553 5 Discussion

554 5.1 The role of rainfall simulations in watershed-scale models

555 Rainfall simulation is a widely used tool to infer local scale infiltration parameters and
556 characteristics. Orthogonal photos are an excellent way to gather additional information about
557 runoff characteristics, like inundation and flow paths relative to microtopography. The
558 method of deriving inundated area fractions is particularly useful, because they can be directly
559 linked to depth-discharge relationships (Equations 4 and 7). Despite some inter year
560 variability, calculated depths and effective runoff show a clear relationship (Figure 7). The
561 range of average depth values ($< 1 - 7$ mm) lies within the range that Abrahams and Parsons
562 [44] measured at a similar site on the WGEW. Direct, high precision measurements of runoff
563 water depth [45] or combined inundation and microtopographical measurements for the
564 calculation of water depth are surely superior to inference from flow velocity. However, even
565 in the absence of more direct depth measurements, taking inundation into account will yield
566 more realistic average water depths than the sheet flow assumption, because flow on a small
567 scale hardly ever covers the whole surface where microtopography is present [46].

568 Values of Manning's n calibrated from the natural rainfall-runoff events were lower with
569 a factor of 3 for the CON model and 19 for the WDD model compared to values derived from
570 rainfall simulations, and K_e and μ_K were four to five times lower (Table 2). There are several
571 possible explanations for this discrepancy, but none taken on its own is sufficient. Regarding
572 hydraulic roughness, it was observed from the orthogonal photos that plot borders impeded
573 flow around mounds of creosote bushes. This must have led to more inundation and higher
574 water depths than would occur in a natural setting without plot borders, where flow can
575 follow unimpeded low lying channels between mounds. This means that on the plot average
576 flow velocities were lower and Manning's n higher than in a natural setting. Certainly, the

577 plot borders increase ponding and with it final infiltration rates during rainfall simulations, but
1
2 578 it is unlikely that the effect can explain a four to five -fold difference. Runoff experiments in
3
4 579 2004 still had roughly 2.5 times higher final infiltration rates than the calibrated values.
5
6
7 580 Higher infiltration rates are a common observation for rotating or oscillating boom rainfall
8
9
10 581 simulators. Risse et al. [47] and Nearing et al. [48] have reported 2-4 times higher K_e for
11
12 582 rainfall simulations than calibrated values from runoff measurements on larger scale for
13
14 583 humid environments. Burns [49] reported for the WGEW site 3-6 times higher rainfall
15
16 584 simulation derived K_e than were calibrated for the small watershed-scale. The source of this
17
18
19 585 discrepancy has not been reported. Beside the plot border effect, we can briefly point out three
20
21
22 586 areas of explanation that can contribute to the difference. First, the oscillating boom rainfall
23
24 587 simulator has intermittent, very high rainfall intensities with no rainfall in between. According
25
26 588 to the partial area response concept, during the high rainfall intensity bursts, high infiltration
27
28
29 589 rates can be achieved, while only time-averaged rainfall intensity is reported that would lead
30
31
32 590 to a much lower infiltration rate. Secondly, there could be a bias during rainfall simulation
33
34 591 site selection towards higher infiltration 'interrill' areas. Finally, during rainfall simulations
35
36 592 air can escape laterally, which is not possible under natural rainfall which covers the whole
37
38
39 593 area.

40
41 594 As infiltration was higher on the small rainfall simulation-scale, scale effects were the
42
43
44 595 inverse of what one would expect from runoff-infiltration theory. But given the above-
45
46 596 mentioned differences between rainfall simulations and watershed-scale natural rainfall runoff
47
48
49 597 measurements that can possibly affect infiltration rates, it can be concluded that the two types
50
51 598 are incomparable for the purpose of scale enquiry, at least under the studied conditions and
52
53
54 599 environment. This implies that rainfall simulations cannot simply be used for the
55
56 600 parameterization of any of the two predictive models, which is confirmed by their bad
57
58 601 performance when parameterized with rainfall simulation data in this study. Nevertheless,
59

602 rainfall simulations can be a valuable tool to study depth-discharge relationships, and relative
603 differences of infiltration between sites and environments, or indeed to study any sub-
604 processes of infiltration in more detail.

605

606 5.2 Importance of water depth-dependency and runoff infiltration

607 Both models can predict hydrographs satisfactorily when calibrated on the watershed-
608 scale (Table 3). The water depth-dependent model (WDD) performs slightly better than the
609 conventional sheet flow model (CON), but this improvement is not related to the inundation
610 effect, as the effect is probably very small when parameterized with a relatively low
611 Manning's n of 0.028 (Figure 10). Possibly, the main improvement above CON stems from
612 the responsiveness of runoff to rainfall, because WDD contains a distribution of hydraulic
613 conductivities, where low conductivities already respond with runoff production at low
614 rainfall intensities. For the CON model, the inclusion of runoff infiltration improves
615 performance slightly (Table 3). This supports the theoretical importance of runoff infiltration
616 pointed out already by other researchers [10, 13].

617 There are three model structural reasons and one physical reason why water depth-
618 dependent infiltration and runoff infiltration does not show up to be important in the WDD
619 model in this study. First, Langhans et al. [27] have shown in a synthetic study that scale
620 effects due to the water depth effect can be significant, but they used a relatively high
621 hydraulic roughness value derived from rainfall simulations. In this study, hydraulic
622 roughness is relatively low, and significant water depths that cause water depth-dependent
623 infiltration do not build up. The physical reason, related to this, is that the macrotopography in
624 the study catchment is very rugged so that runoff concentrates very quickly in channels and
625 the effective hillslope lengths are very short; water depth cannot build up sufficiently on such

626 short slopes. The second model structural reason is that the exponential distribution assumed
1
2 627 here (Equation 8) is such that only at high inundation levels significant infiltration can occur.
3
4 628 If a different distribution had been chosen the water depth effect could have been more
5
6
7 629 pronounced, such as the log-normal distribution which had been suggested before for
8
9
10 630 variation of K_{sat} at larger scales [50-52]. But the analytical solution of the concept described
11
12 631 here (i.e. Equations 8 – 16) is not applicable to all distributions and it would require a more
13
14 632 stochastic, quasi-empirical approach to formulate the model with empirical or more complex
15
16 633 distributions. The third model structural reason is that the assumption that hydraulic
17
18
19 634 conductivities are strictly monotonously increasing within the microtopography is probably
20
21
22 635 too strict. Some randomness within a modelling cell, and between would increase the chance
23
24 636 of runoff infiltration. A full study of various model structure-related effects, such as the choice
25
26 637 of distribution, cell resolution, or randomness would be desirable but is beyond the scope of
27
28
29 638 this study, as most would require a significant reformulation of the model. Consequently, and
30
31 639 despite strong theoretical justification of the water depth-dependent infiltration process as
32
33
34 640 pointed out in the introduction, the evidence for the water depth effect remains inconclusive
35
36 641 from this study. Future research into the water depth effect and runoff infiltration should
37
38
39 642 therefore occur under more controlled field conditions that are tailored to quantify locations
40
41 643 and flow pathways during infiltration. Only then it is reasonable to include these effects into
42
43
44 644 models for prediction purpose.

645

50 646 6 Conclusions

51
52
53
54 647 The pattern of high infiltrability areas on mounds underneath shrubs and lower lying low
55
56
57 648 infiltrability areas in the inter-shrub area has previously been demonstrated for semi-arid
58
59

649 rangeland. Within the concept of water depth-dependent infiltration, runoff accumulation
1
2 650 further downslope leads to increased water depth inundating high infiltrability areas, which
3
4
5 651 increases the area average infiltration rate, one of many explanations for observed scale
6
7 652 effects in runoff and erosion. A model was developed that combines the concepts of water
8
9
10 653 depth-dependent infiltration, partial contributing area under variable rainfall intensity, and the
11
12 654 Green-Ampt theory for point-scale infiltration. The model was applied to rainfall simulation
13
14
15 655 data and natural rainfall – runoff data from a small semiarid watershed (0.4 ha) in the US
16
17 656 Southwest. The model performance was compared to the performance of a conventional
18
19 657 Green-Ampt model with the sheet flow assumption. Both models were parameterized with
20
21
22 658 rainfall simulation data, and by calibration from watershed-scale runoff measurements.
23
24 659 Parameters of hydraulic roughness and conductivity were larger by a high multiple for the
25
26
27 660 former compared to the latter. This implies that scale effects were the inverse of the
28
29 661 expectation, and rainfall simulation plot-scale data could not be used to successfully predict
30
31
32 662 hydrographs. Calibrated models both had good performance, with the water depth-dependent
33
34 663 model being slightly better. While runoff infiltration was important in improving performance
35
36 664 of the sheet flow assumption model, water depth effect was negligible in the new model. This
37
38
39 665 was explained with rigid assumptions in the model structure, low hydraulic roughness, and
40
41 666 short hillslopes. The proposed model makes some theoretical advancement towards a less
42
43
44 667 scale-dependent way of modelling runoff and erosion on the hillslope-scale, but when
45
46 668 calibrated on the watershed-scale, these structural changes bring little predictive gain.
47
48

49 669
50
51
52
53
54
55
56
57
58
59
60
61
62
63
64
65

670 Acknowledgements

1
2
3
4
5 671 The authors would like to thank the staff of the Southwest Watershed Research Center
6
7 672 (SWRC) in Tucson, AZ and students from the University of Arizona who helped providing
8
9
10 673 rainfall simulation and other data. We would also like to thank the anonymous reviewers who
11
12 674 significantly contributed to the improvement of the first manuscript. The project was funded
13
14 675 by the Flemish Agency for the Promotion of Innovation by Science and Technology (IWT)
15
16
17 676 and by a travel grant of the Research Foundation – Flanders (FWO).
18

19 677
20
21
22
23
24
25
26
27
28
29
30
31
32
33
34
35
36
37
38
39
40
41
42
43
44
45
46
47
48
49
50
51
52
53
54
55
56
57
58
59
60
61
62
63
64
65

678 Notation

1		
2		
3		
4		
5	679	A_c rainfall excess contributing area fraction, -
6		
7	680	A_i flow inundated area fraction, -
8		
9		
10	681	b empirical factor of the inundation-depth relationship, L^{-1}
11		
12	682	CON conventional Green-Ampt model with sheet flow
13		
14	683	D average water depth, L
15		
16		
17	684	Δr unit area net inflow, LT^{-1}
18		
19	685	Δt time step, T
20		
21		
22	686	$\Delta\theta$ difference between initial and saturated volumetric moisture content, $L^3 L^{-3}$
23		
24	687	η_e effective soil porosity, $L^3 L^{-3}$
25		
26		
27	688	f_e effective infiltration rate, LT^{-1}
28		
29	689	f_i potential infiltration rate or infiltrability, LT^{-1}
30		
31		
32	690	F_t cumulative infiltration at the end of a time step, L
33		
34	691	i rainfall intensity, LT^{-1}
35		
36	692	K_c average hydraulic conductivity of runoff contributing area, LT^{-1}
37		
38		
39	693	K_e effective hydraulic conductivity, LT^{-1}
40		
41	694	K_i average hydraulic conductivity of inundated area, LT^{-1}
42		
43		
44	695	K_s point-scale saturated hydraulic conductivity, LT^{-1}
45		
46	696	l_p plot length or modelling unit length, L
47		
48		
49	697	LP Large plot
50		
51	698	m exponent of depth-discharge relationship representing turbulence of flow, -
52		
53		
54	699	ME Model efficiency, -
55		
56	700	μ_f mean of distribution of infiltrabilities, LT^{-1}
57		
58	701	μ_K mean of distribution of K_s , LT^{-1}
59		
60		
61		
62		
63		
64		
65		

702	n	Manning's roughness coefficient, -
703	OBJ	objective function, -
704	P	total precipitation of an event, L
705	ψ	suction across the wetting front and $\Delta\theta$, L
706	Q	discharge during time step, L^3T^{-1}
707	q_e	unit flow width discharge, plot length-averaged, L^2T^{-1}
708	Q_e	steady state effective discharge, L^3T^{-1}
709	Q_p	peak discharge, L^3T^{-1}
710	Q_t	total discharge, L^3
711	R^2	Coefficient of determination, -
712	r_e	rainfall and runoff excess or unit area flow rate, plot-averaged, LT^{-1}
713	r_{in}	unit area inflow rate at upper plot boundary, LT^{-1}
714	ρ_b	bulk density, ML^{-3}
715	r_{out}	unit area outflow rate at lower plot boundary, LT^{-1}
716	S	slope gradient, -
717	SP	small plots
718	t	time, -
719	θ_i	initial volumetric soil moisture content, before start of rain, L^3L^{-3}
720	θ_w	volumetric soil moisture content, L^3L^{-3}
721	u	average runoff velocity, LT^{-1}
722	WDD	water depth-dependent Green-Ampt model with partial inundation
723	w_p	plot width, L

724 Reference list

- 725 [1] Joel A, I Messing, O Seguel, M Casanova. Measurement of surface water runoff from
726 plots of two different sizes. *Hydrol Process*. 16 (2002) 1467-78, doi: DOI 10.1002/hyp.356.
- 727 [2] Yair A, N Raz-Yassif. Hydrological processes in a small and catchment: scale effects of
728 rainfall and slope length. *Geomorphology*. 61 (2004) 155-69, doi: DOI
729 10.1016/j.geomorph.2003.12.003.
- 730 [3] Cerdan O, Y Le Bissonnais, G Govers, V Lecomte, K van Oost, A Couturier, et al. Scale
731 effect on runoff from experimental plots to catchments in agricultural areas in Normandy.
732 *Journal of Hydrology*. 299 (2004) 4-14, doi: DOI 10.1016/j.jhydrol.2004.02.017.
- 733 [4] Lal R. Soil degradative effects of slope length and tillage methods on alfisols in western
734 Nigeria .1. Runoff, erosion and crop response. *Land Degradation & Development*. 8 (1997)
735 201-19.
- 736 [5] Le Bissonnais Y. Crusting, runoff and sheet erosion on silty loamy soils at various scales
737 and upscaling from m² to small catchments. *Soil & Tillage Research*. 46 (1998) 69-80.
- 738 [6] Parsons AJ, RE Brazier, J Wainwright, DM Powell. Scale relationships in hillslope runoff
739 and erosion. *Earth Surface Processes and Landforms*. 31 (2006) 1384-93, doi: Doi
740 10.1002/Esp.1345.
- 741 [7] van de Giesen NC, TJ Stomph, N de Ridder. Scale effects of Hortonian overland flow and
742 rainfall-runoff dynamics in a West African catena landscape. *Hydrol Process*. 14 (2000) 165-
743 75.
- 744 [8] Stomph TJ, N De Ridder, TS Steenhuis, NC van de Giesen. Scale effects of Hortonian
745 overland flow and rainfall-runoff dynamics: Laboratory validation of a process-based model.
746 *Earth Surface Processes and Landforms*. 27 (2002) 847-55, doi: Doi 10.1002/Esp.356.
- 747 [9] Wainwright J, AJ Parsons. The effect of temporal variations in rainfall on scale
748 dependency in runoff coefficients. *Water Resources Research*. 38 (2002) -, doi: Doi
749 10.1029/2000wr000188.
- 750 [10] Smith RE. Infiltration theory for hydrologic applications, American Geophysical Union,
751 Washington D.C., 2002.
- 752 [11] Woolhiser DA, DC Goodrich. Effect of storm rainfall intensity patterns on surface
753 runoff. *Journal of Hydrology*. 102 (1988) 335-54.
- 754 [12] Wood EF, M Sivapalan, K Beven. Scale effects in infiltration and runoff production.
755 *Conjunctive Water Use: Proceedings of the Budapest Symposium, July 1986. IAHS1986.*
- 756 [13] Corradini C, R Morbidelli, F Melone. On the interaction between infiltration and
757 Hortonian runoff. *Journal of Hydrology*. 204 (1998) 52-67.
- 758 [14] Govindaraju RS, N Nahar, C Corradini, R Morbidelli. Role of run-on for describing
759 field-scale infiltration and overland flow over spatially variable soils. *Journal of Hydrology*.
760 286 (2004) 36-51, doi: 10.1016/j.jhydrol.2003.09.011.
- 761 [15] Morbidelli R, C Corradini, RS Govindaraju. A field-scale infiltration model accounting
762 for spatial heterogeneity of rainfall and soil saturated hydraulic conductivity. *Hydrol Process*.
763 20 (2006) 1465-81, doi: Doi 10.1002/Hyp.5943.
- 764 [16] Brooks ES, J Boll, PA McDaniel. A hillslope-scale experiment to measure lateral
765 saturated hydraulic conductivity. *Water Resources Research*. 40 (2004) pp.10, doi: Artn
766 W04208
767 Doi 10.1029/2003wr002858.

- 768 [17] Van Nieuwenhuysen B, M Antoine, G Wyseure, G Govers. Pattern-process
1 769 relationships in surface hydrology: hydrological connectivity expressed in landscape metrics.
2 770 *Hydrological Processes*. 25 (2011) 3760-73, doi: 10.1002/hyp.8101.
- 3 771 [18] Lyford FP, HK Qashu. Infiltration Rates as Affected by Desert Vegetation. *Water*
4 772 *Resources Research*. 5 (1969) 1373-6, doi: 10.1029/WR005i006p01373.
- 5 773 [19] Johnson CW, ND Gordon. Runoff and erosion from rainfall simulator plots on sagebrush
6 774 rangeland. *Transactions of the ASAE*. 31 (1988) 421-7.
- 7 775 [20] Bochet E, J Poesen, JL Rubio. Mound development as an interaction of individual plants
8 776 with soil, water erosion and sedimentation processes on slopes. *Earth Surface Processes and*
9 777 *Landforms*. 25 (2000) 847-67, doi: 10.1002/1096-9837(200008)25:8<847::aid-
10 778 esp103>3.0.co;2-q.
- 11 779 [21] Bochet E, JL Rubio, J Poesen. Modified topsoil islands within patchy Mediterranean
12 780 vegetation in SE Spain. *Catena*. 38 (1999) 23-44.
- 13 781 [22] Dunne T, WH Zhang, BF Aubry. Effects of Rainfall, Vegetation, and Microtopography
14 782 on Infiltration and Runoff. *Water Resources Research*. 27 (1991) 2271-85.
- 15 783 [23] Cammeraat LH. A review of two strongly contrasting geomorphological systems within
16 784 the context of scale. *Earth Surface Processes and Landforms*. 27 (2002) 1201-22, doi:
17 785 10.1002/esp.421.
- 18 786 [24] Bresson LM, C Valentin. Soil surface crust formation - contribution of
19 787 micromorphology. in: AJ Ringrose-Voase, GS Humphreys, (Eds.). *Soil Micromorphology:*
20 788 *Studies in Management and Genesis*. Elsevier Science Publ B V, Amsterdam, 1994. pp. 737-
21 789 62.
- 22 790 [25] Fox DM, Y Le Bissonnais, A Bruand. The effect of ponding depth on infiltration in a
23 791 crusted surface depression. *Catena*. 32 (1998) 87-100.
- 24 792 [26] Langhans C, G Govers, J Diels, W Clymans, A Van den Putte. Dependence of effective
25 793 hydraulic conductivity on rainfall intensity: loamy agricultural soils. *Hydrological Processes*.
26 794 24 (2010) 2257-68.
- 27 795 [27] Langhans C, G Govers, J Diels. Development and parameterization of an infiltration
28 796 model accounting for water depth and rainfall intensity. *Hydrological Processes*. 27 (2013)
29 797 3777-90, doi: 10.1002/hyp.9491.
- 30 798 [28] Langhans C, G Govers, J Diels, A Leys, W Clymans, AVd Putte, et al. Experimental
31 799 rainfall-runoff data: Reconsidering the concept of infiltration capacity. *Journal of Hydrology*.
32 800 399 (2011) 255-62.
- 33 801 [29] Blöschl G, M Sivapalan. Scale issues in hydrological modelling: A review. *Hydrological*
34 802 *Processes*. 9 (1995) 251-90, doi: Doi 10.1002/hyp.3360090305.
- 35 803 [30] Stone JJ, MH Nichols, DC Goodrich, J Buono. Long-term runoff database, Walnut
36 804 Gulch Experimental Watershed, Arizona, United States. *Water Resources Research*. 44
37 805 (2008) 1-5, doi: Artn W05s05
38 806 Doi 10.1029/2006wr005733.
- 39 807 [31] Osterkamp WR. Geology, soils, and geomorphology of the Walnut Gulch Experimental
40 808 Watershed, Tombstone, Arizona. *Journal of the Arizona-Nevada Academy of Science*. 40
41 809 (2008) 136-54.
- 42 810 [32] Paige GB, JJ Stone, JR Smith, JR Kennedy. The walnut gulch rainfall simulator: A
43 811 computer-controlled variable intensity rainfall simulator. *Applied Engineering in Agriculture*.
44 812 20 (2004) 25-31.
- 45 813 [33] Stone JJ, GB Paige, RH Hawkins. Rainfall intensity-dependent infiltration rates on
46 814 rangeland rainfall simulator plots. *Transactions of the ASAE*. 51 (2008) 45-53.
- 47 815 [34] Luk SH, W Merz. Use of the salt tracing technique to determine the velocity of
48 816 overland-flow. *Soil Technology*. 5 (1992) 289-301.

- 817 [35] Green WH, GA Ampt. Studies on soil physics, 1. The flow of air and water through
1 818 soils. *Journal of Agricultural Sciences*. 4 (1911) 1-22.
- 2 819 [36] Chow VT, DR Maidment, LW Mays. *Applied Hydrology*. McGraw-Hill, New York,
3 820 1988.
- 4 821 [37] Chu ST. Infiltration during an Unsteady Rain. *Water Resources Research*. 14 (1978)
5 822 461-6.
- 6 823 [38] Emmett WW. Overland flow. in: MJ Kirkby, (Ed.). *Hillslope Hydrology*. Wiley, New
7 824 York, 1978. pp. 145-76.
- 8 825 [39] Hawkins RH. Interpretation of source area variability in rainfall-runoff relations. *Proc,*
9 826 *Int Symp on Rainfall-Runoff Modeling*, Mississippi State Univ., Mississippi State, 1982. pp.
10 827 303-24.
- 11 828 [40] Yu B, U Cakurs, CW Rose. An assessment of methods for estimating runoff rates at the
12 829 plot scale. *Transactions of the ASAE*. 41 (1998) 653-61.
- 13 830 [41] Chen ZQ, RS Govindaraju, ML Kavvas. Spatial averaging of unsaturated flow equations
14 831 under infiltration conditions over areally heterogeneous fields. 2. Numerical simulations.
15 832 *Water Resources Research*. 30 (1994) 535-48.
- 16 833 [42] Polyakov VO, A Kimoto, MA Nearing, MH Nichols. Tracing Sediment Movement on a
17 834 Semiarid Watershed using Rare Earth Elements All rights reserved. No part of this periodical
18 835 may be reproduced or transmitted in any form or by any means, electronic or mechanical,
19 836 including photocopying, recording, or any information storage and retrieval system, without
20 837 permission in writing from the publisher. Permission for printing and for reprinting the
21 838 material contained herein has been obtained by the publisher. *Soil Sci Soc Am J*. 73 (2009)
22 839 1559-65, doi: 10.2136/sssaj2008.0378.
- 23 840 [43] Yu B, CW Rose, CAA Ciesiolka, KJ Coughlan, B Fentie. Toward a framework for
24 841 runoff and soil loss prediction using GUEST technology. *Australian Journal of Soil Research*.
25 842 35 (1997) 1191-212.
- 26 843 [44] Abrahams AD, AJ Parsons. Determining the mean depth of overland flow in field
27 844 studies of flow hydraulics. *Water Resour Res*. 26 (1990) 501-3, doi:
28 845 10.1029/WR026i003p00501.
- 29 846 [45] Dunkerley D. Estimating the mean speed of laminar overland flow using dye injection-
30 847 uncertainty on rough surfaces. *Earth Surface Processes and Landforms*. 26 (2001) 363-74.
- 31 848 [46] Fox DM, RB Bryan, AG Price. The influence of slope angle on final infiltration rate for
32 849 interrill conditions. *Geoderma*. 80 (1997) 181-94.
- 33 850 [47] Risse LM, MA Nearing, XC Zhang. Variability in Green-Ampt effective hydraulic
34 851 conductivity under fallow conditions. *Journal of Hydrology*. 169 (1995) 1-24.
- 35 852 [48] Nearing MA, BY Liu, LM Risse, X Zhang. Curve numbers and Green-Ampt effective
36 853 hydraulic conductivities. *Journal of the American Water Resources Association*. 32 (1996)
37 854 125-36, doi: Doi 10.1111/j.1752-1688.1996.tb03440.x.
- 38 855 [49] Burns ISC. *Reducing uncertainty in hydrological modeling: A step-wise multi-scale*
39 856 *calibration approach [Ms.]*. Tucson, AZ: University of Arizona; 2010.
- 40 857 [50] Sharma ML, GA Gander, CG Hunt. Spatial variability of infiltration in a watershed.
41 858 *Journal of Hydrology*. 45 (1980) 101-22.
- 42 859 [51] Sharma ML, RJW Barron, MS Fernie. Areal distribution of infiltration parameters and
43 860 some soil physical properties in lateritic catchments. *Journal of Hydrology*. 94 (1987) 109-27,
44 861 doi: 10.1016/0022-1694(87)90035-7.
- 45 862 [52] Smith RE, DC Goodrich. Model For Rainfall Excess Patterns on Randomly
46 863 Heterogeneous Areas. *Journal of Hydrologic Engineering*. 5 (2000) 355-62.
- 47 864
48 865

866 Figure captions

867

868 Figure 1: Location of the study site in the southwest United States

869 Figure 2: Contour map of watershed LH- 106 in the Lucky Hills Study Area (Figure 1) with a

870 0.2 m contour interval. The background is a panchromatic Quickbird image from 7. July

871 2010. Geographic coordinates of the centre of the catchment are $31^{\circ}44'32''N$, $110^{\circ}03'14''W$

872 Figure 3: Creosote bush on mound and stony inter-shrub area.

873 Figure 4: Flow chart of the CON model and the calibration procedure with multiple rainfall

874 events. Numbers in brackets refer to Equations.

875 Figure 5a: Schematic representation of a surface unit during the beginning and middle phase

876 of a rainstorm, when $A_c > A_i$. Rainfall excess erratically flows down the microtopographic

877 slope towards the low conductivity area where inundation starts.

878 Figure 5b: Schematic representation of a surface unit during the recession or directly after a

879 rainstorm in an area where runoff concentrates or accumulates, where inundated area (A_i)

880 dominates infiltration.

881 Figure 6: Flow chart of the WDD model and the calibration procedure with multiple rainfall

882 events. Numbers in brackets refer to Equations.

883 Figure 7: Relationship between average water depth and effective discharge for 2007 and

884 2008 on the rainfall simulation plots. In the CON model water depth is calculated for the

885 whole plot width, while in the WDD model it is calculated for the inundated area only.

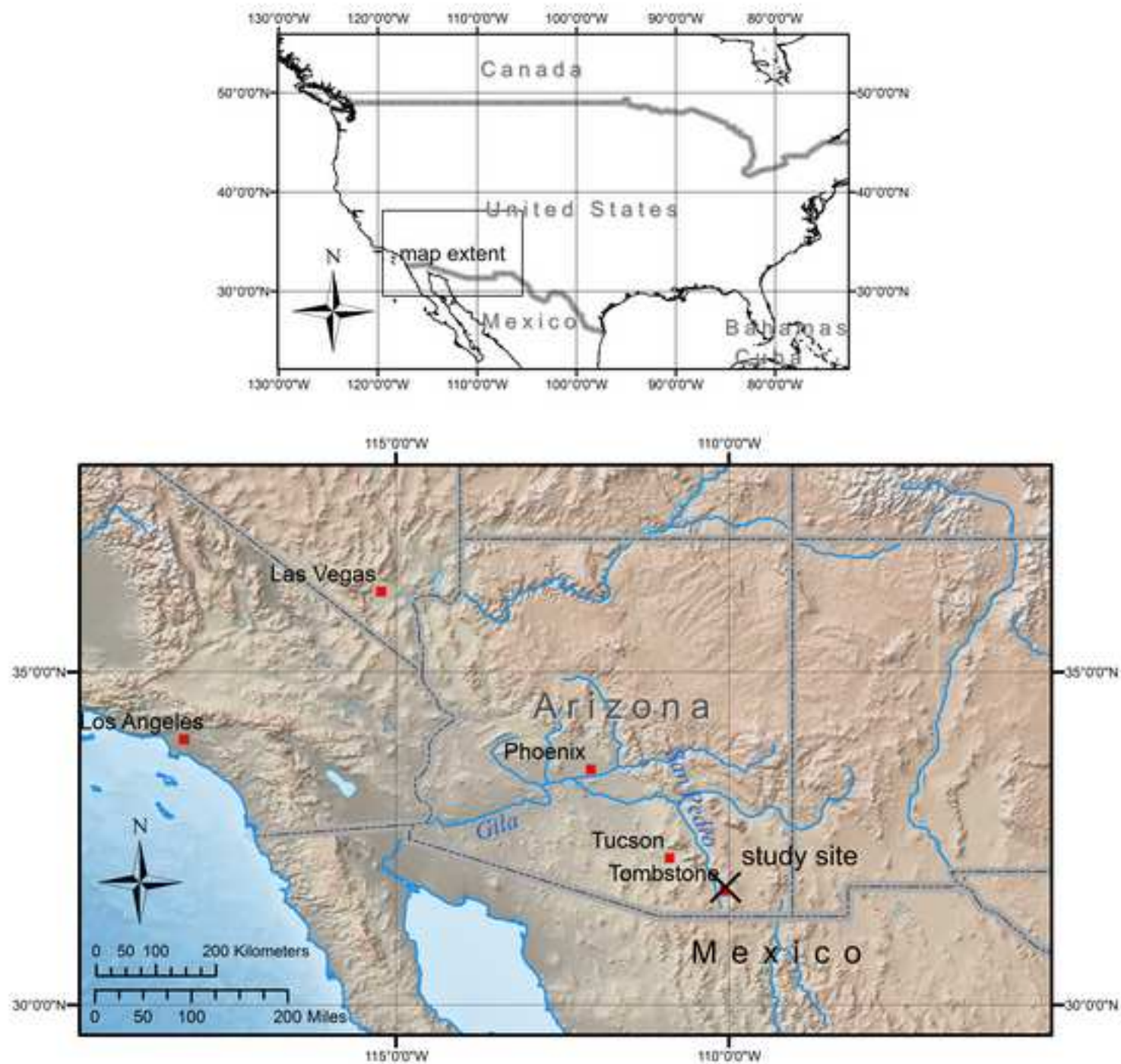
1
2
3
4
5
6
7
8
9
10
11
12
13
14
15
16
17
18
19
20
21
22
23
24
25
26
27
28
29
30
31
32
33
34
35
36
37
38
39
40
41
42
43
44
45
46
47
48
49
50
51
52
53
54
55
56
57
58
59
60
61
62
63
64
65

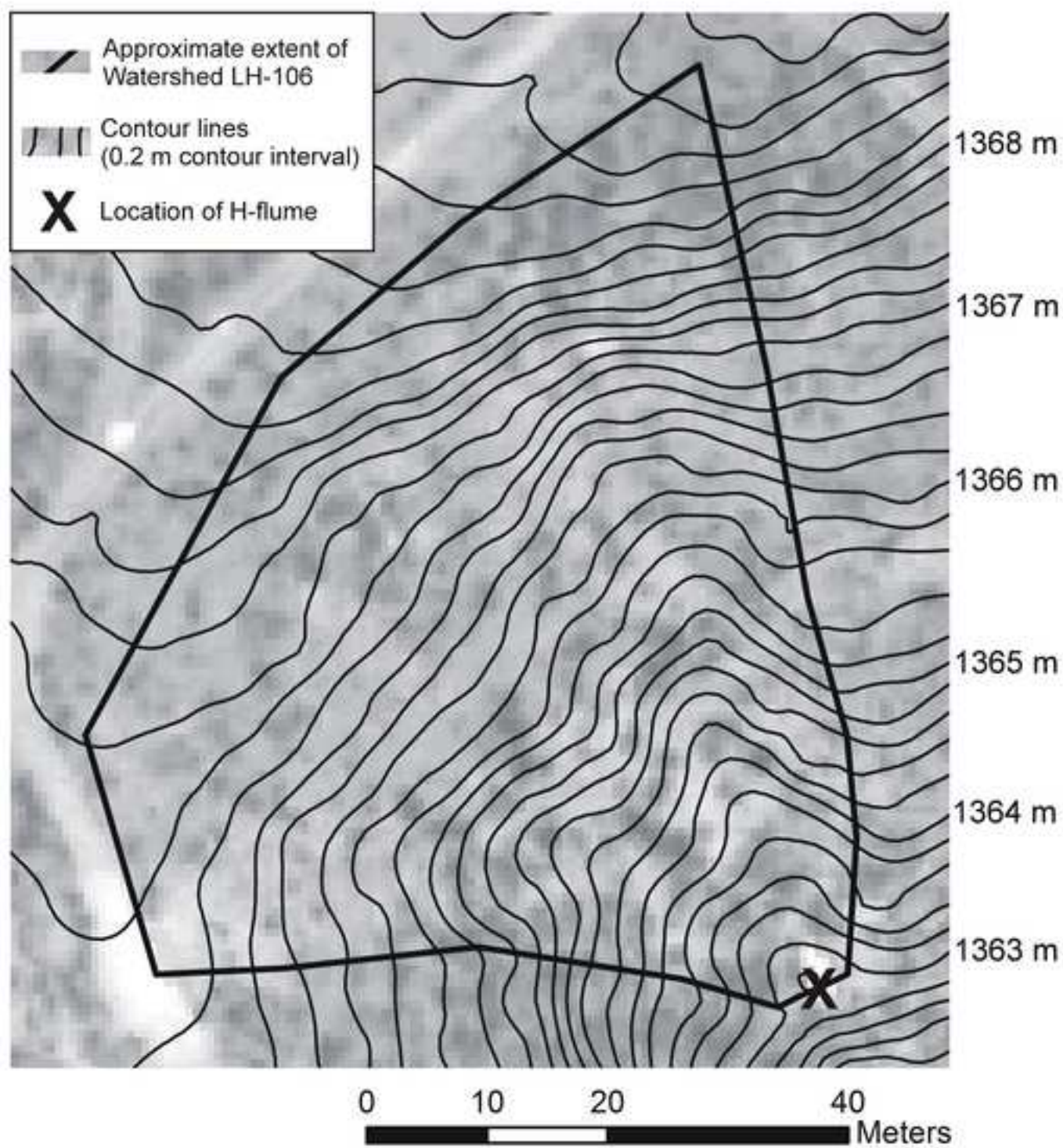
886 Figure 8: Relationship between observed final infiltration rates and rainfall intensity under
887 simulated rainfall. Lines are modelled averages of the CON model (dotted), the WDD model
888 without runoff infiltration (dashed), and the WDD model with runoff infiltration (solid).

889 Figure 9: Contour plots of the OBJ value in the parameter space: a) Manning's n vs. K_e for
890 CON, b) ψ vs. K_e for CON, c) Manning's n vs. μK for WDD, d) ψ vs. μK for WDD

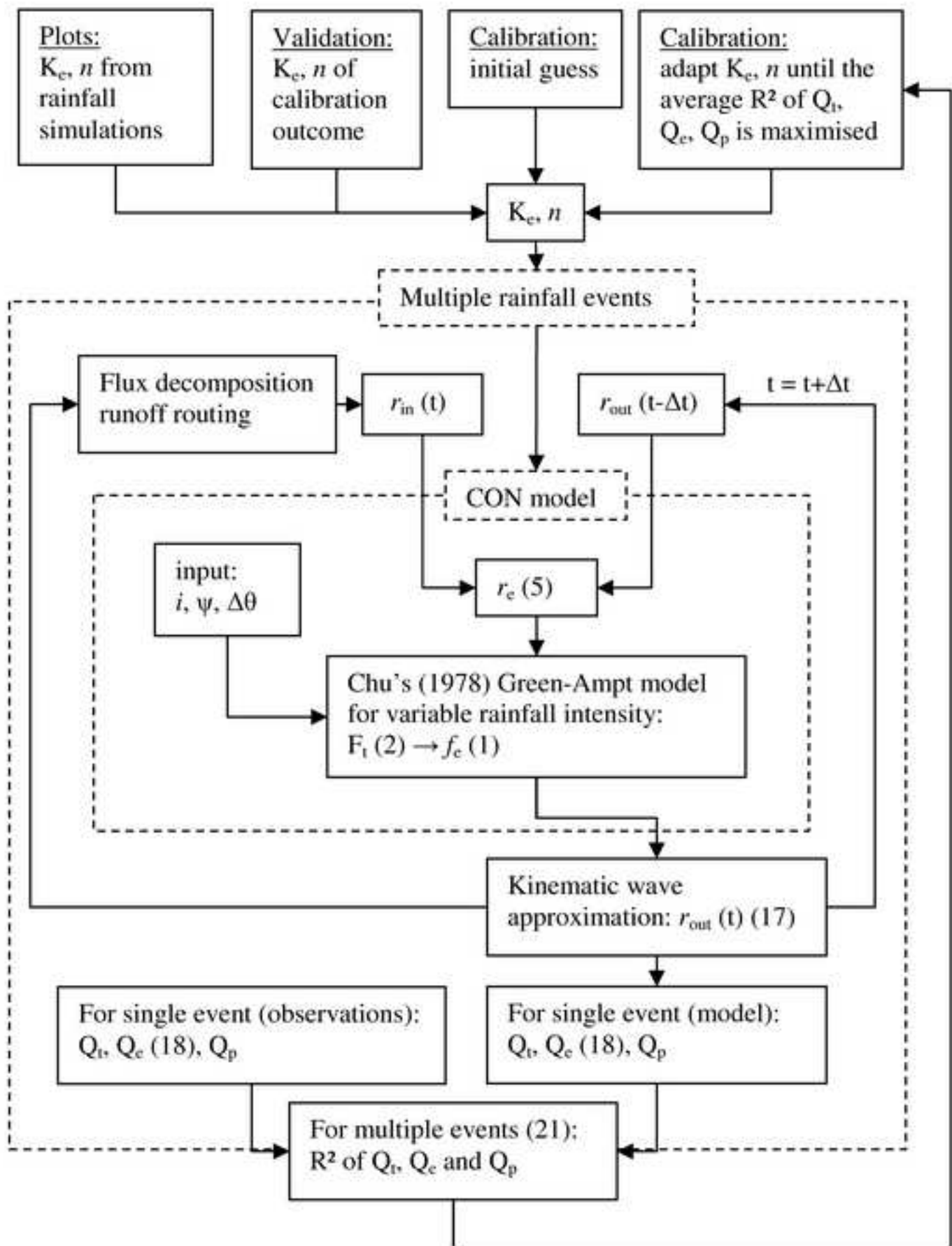
891 Figure 10: Catchment average infiltration rate vs. time for a synthetic 30 min storm with 40
892 mm h⁻¹ rainfall intensity. Infiltration rates of the WDD model with runoff infiltration (solid)
893 and without runoff infiltration (dotted), and of the CON model with runoff infiltration
894 (dashed) and without runoff infiltration (dash-dotted) are shown.

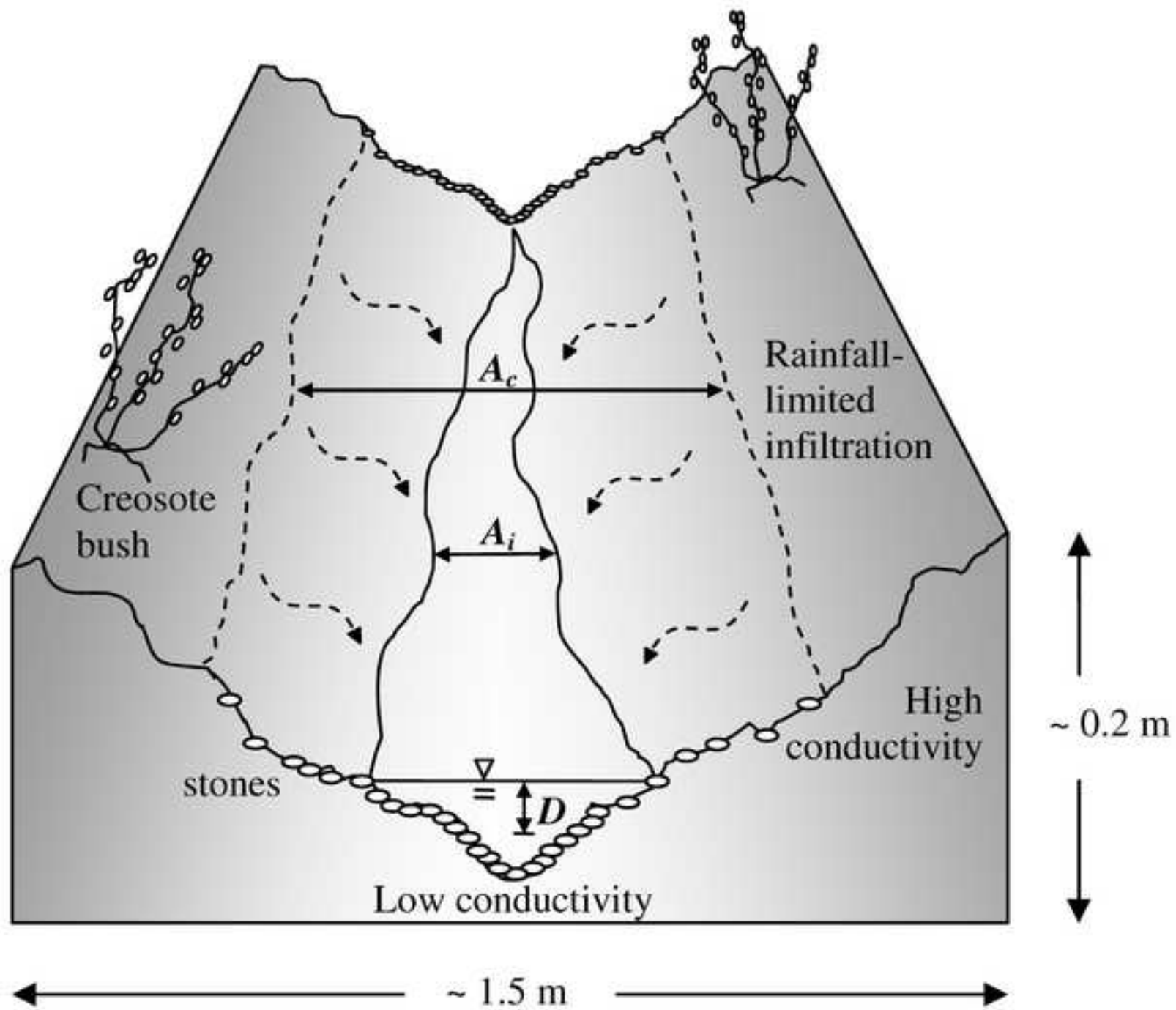
895 Figure 11: Modelled and observed hydrographs of the 90th (a: CON, b: WDD) 50th (c: CON,
896 d: WDD) and 10th (e: CON, f: WDD) percentile events based on descending ranking of ME
897 for the CON and the WDD models. Observed hydrographs are solid-shaded and modelled
898 hydrographs are dashed (WDD) and dash-dotted (CON). Rainfall intensity is displayed as
899 stepped, solid line with an inverted scale on the right.

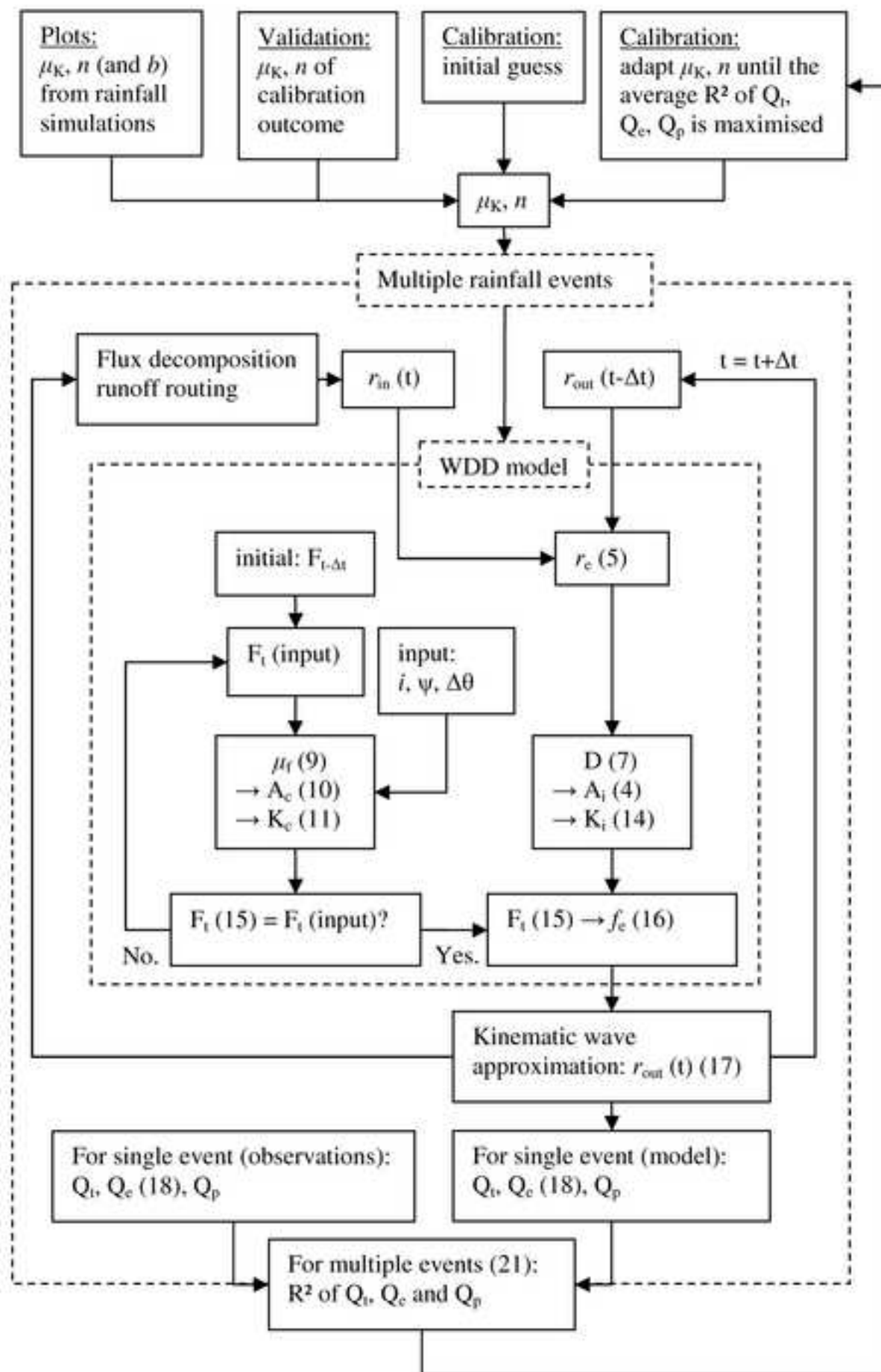












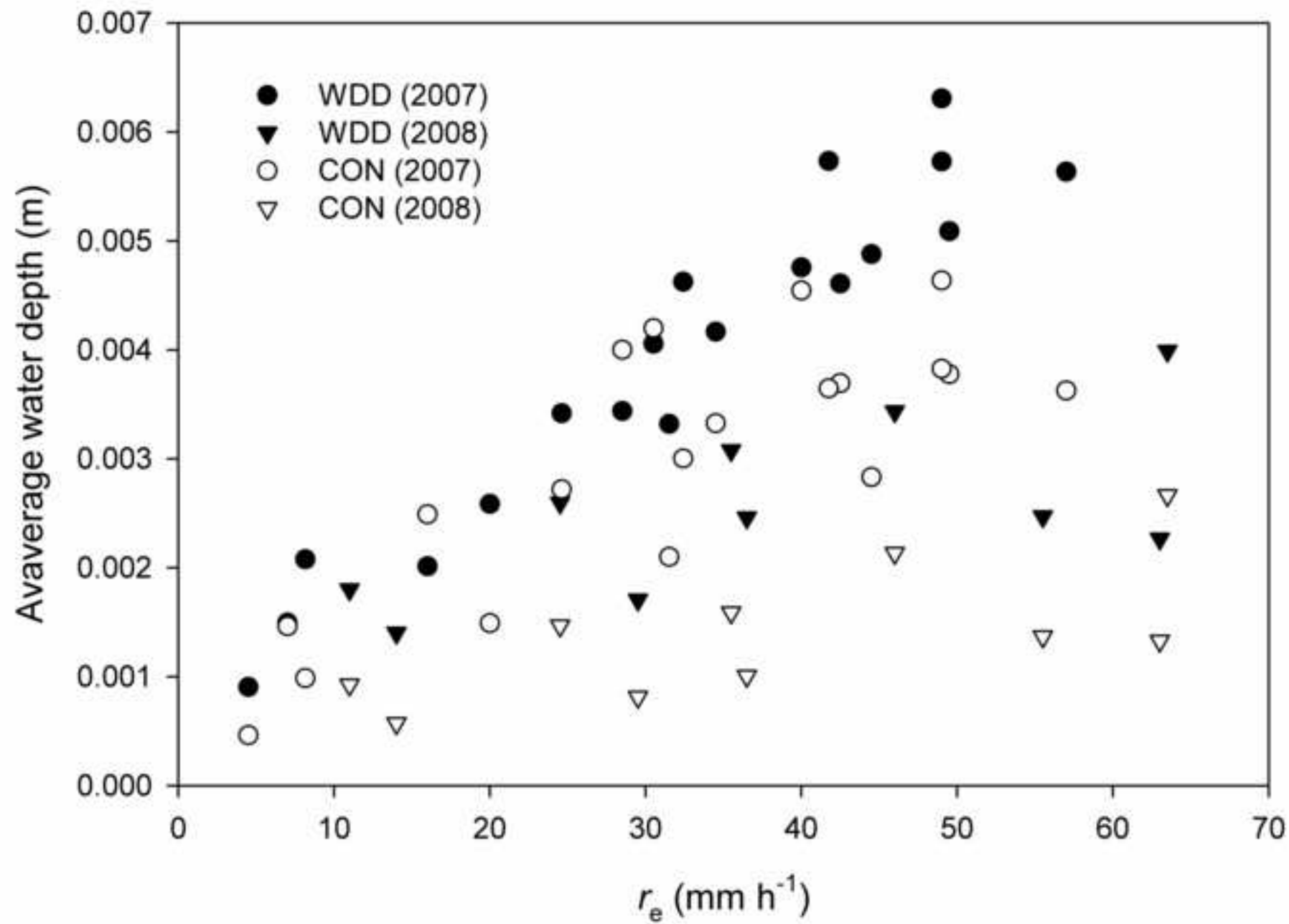
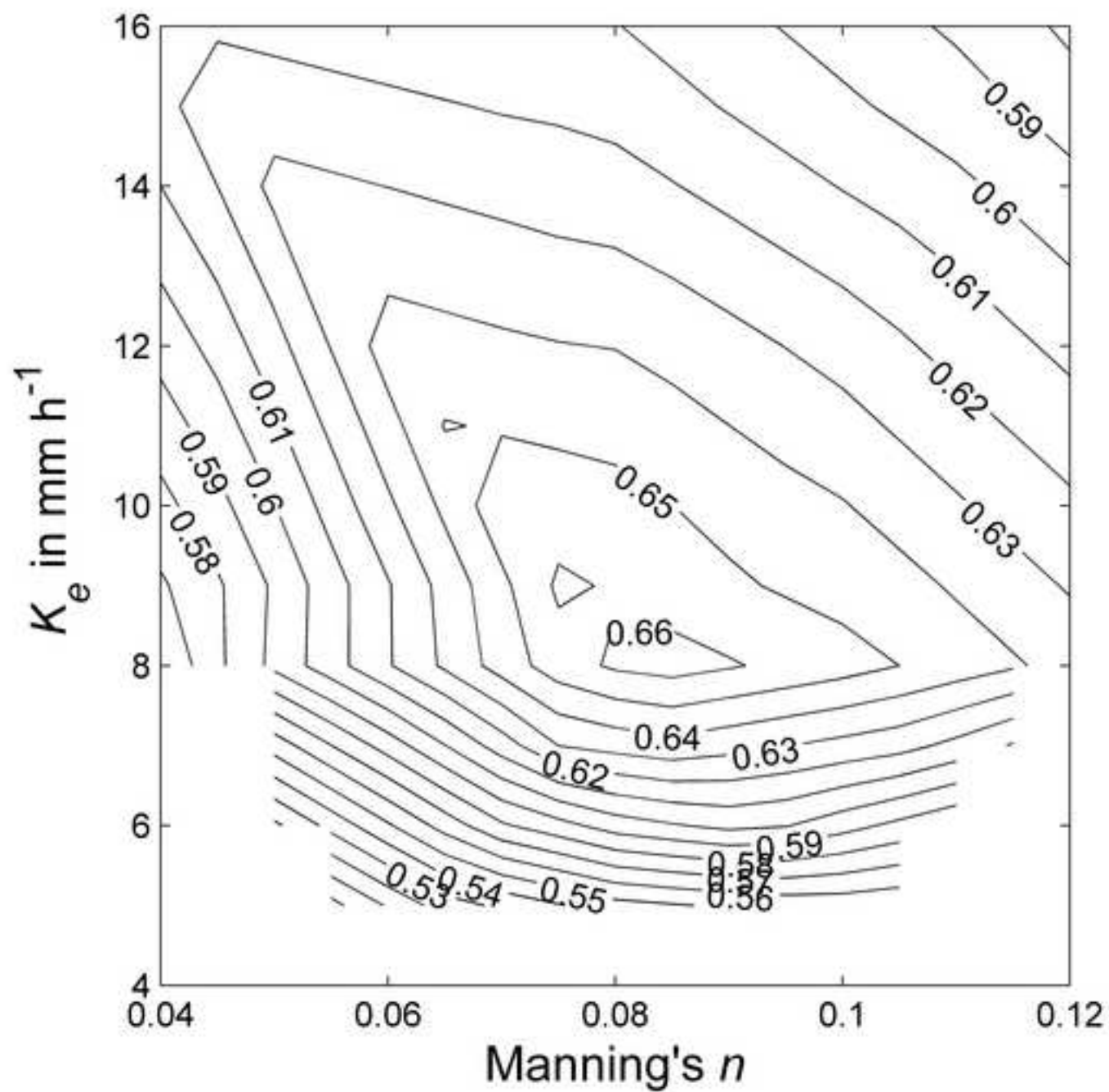
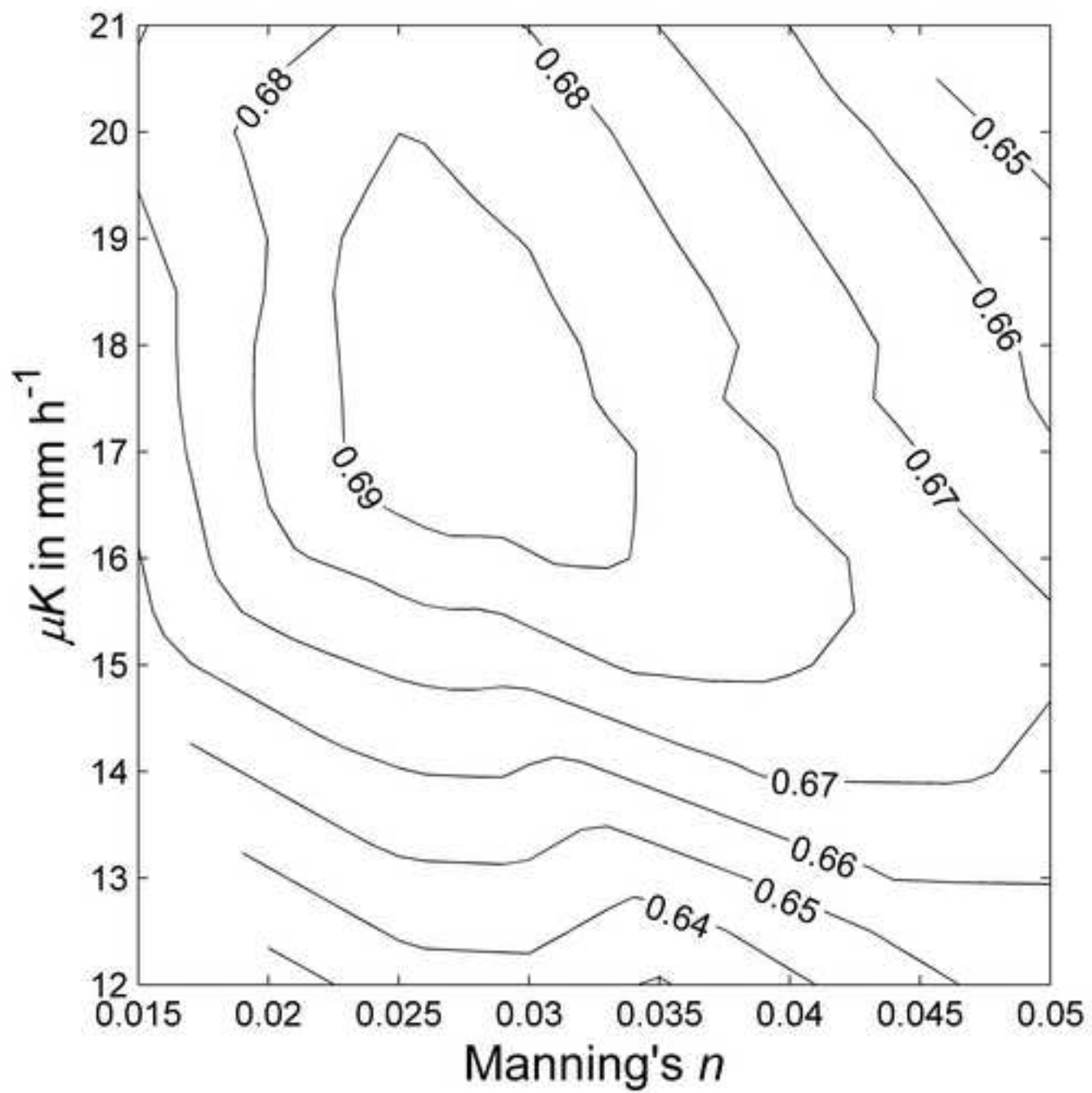
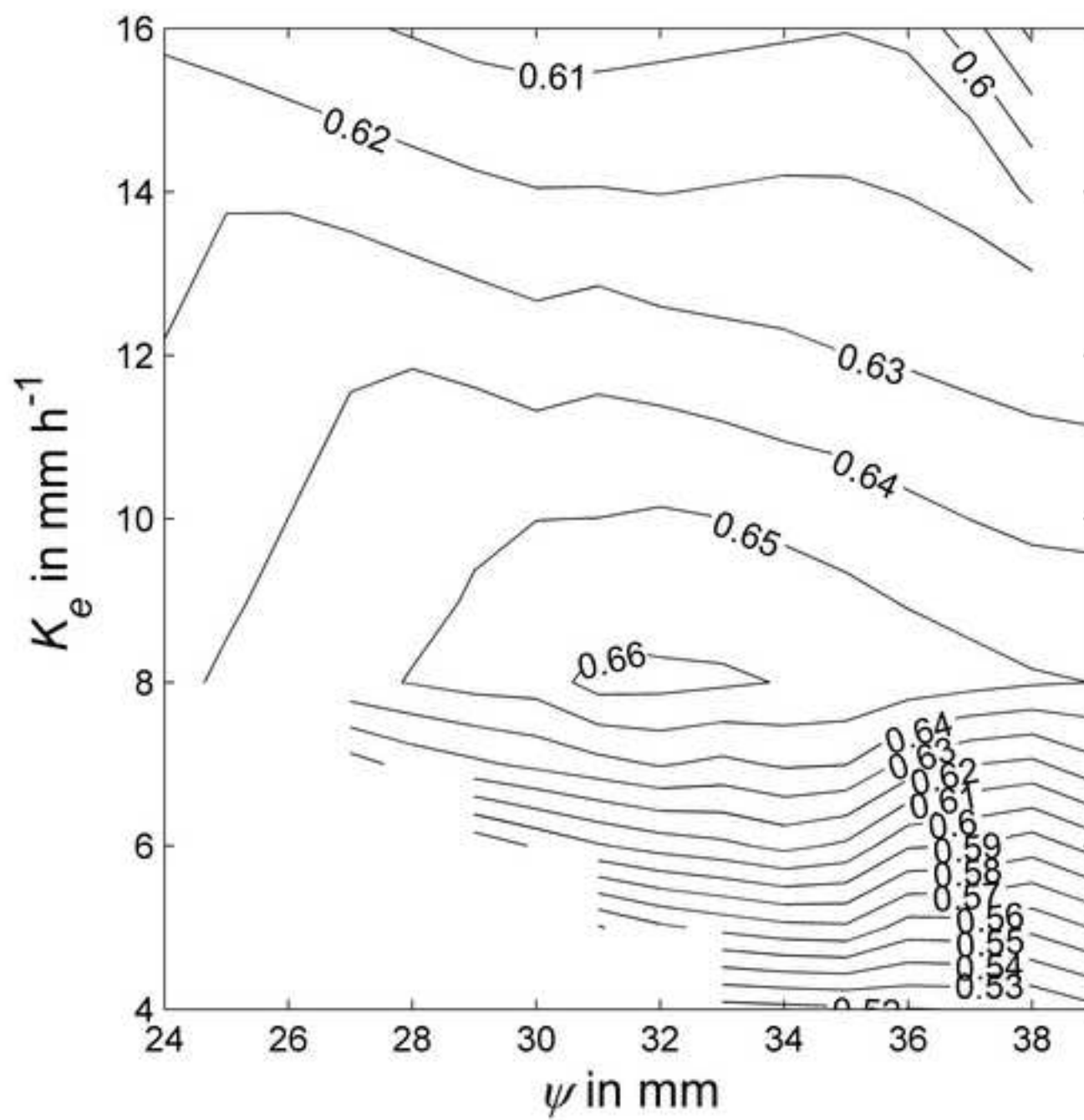


Figure 9a







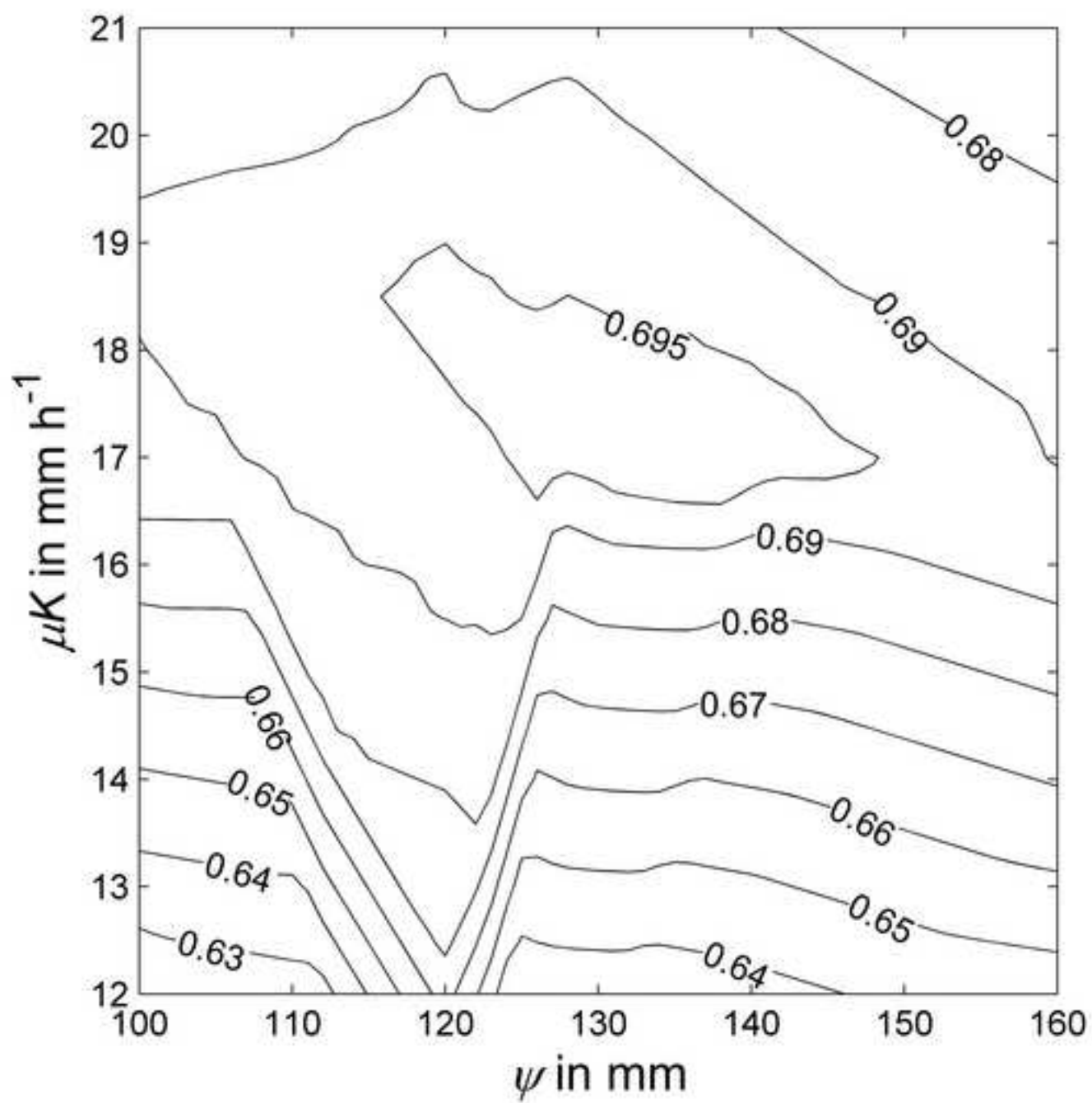
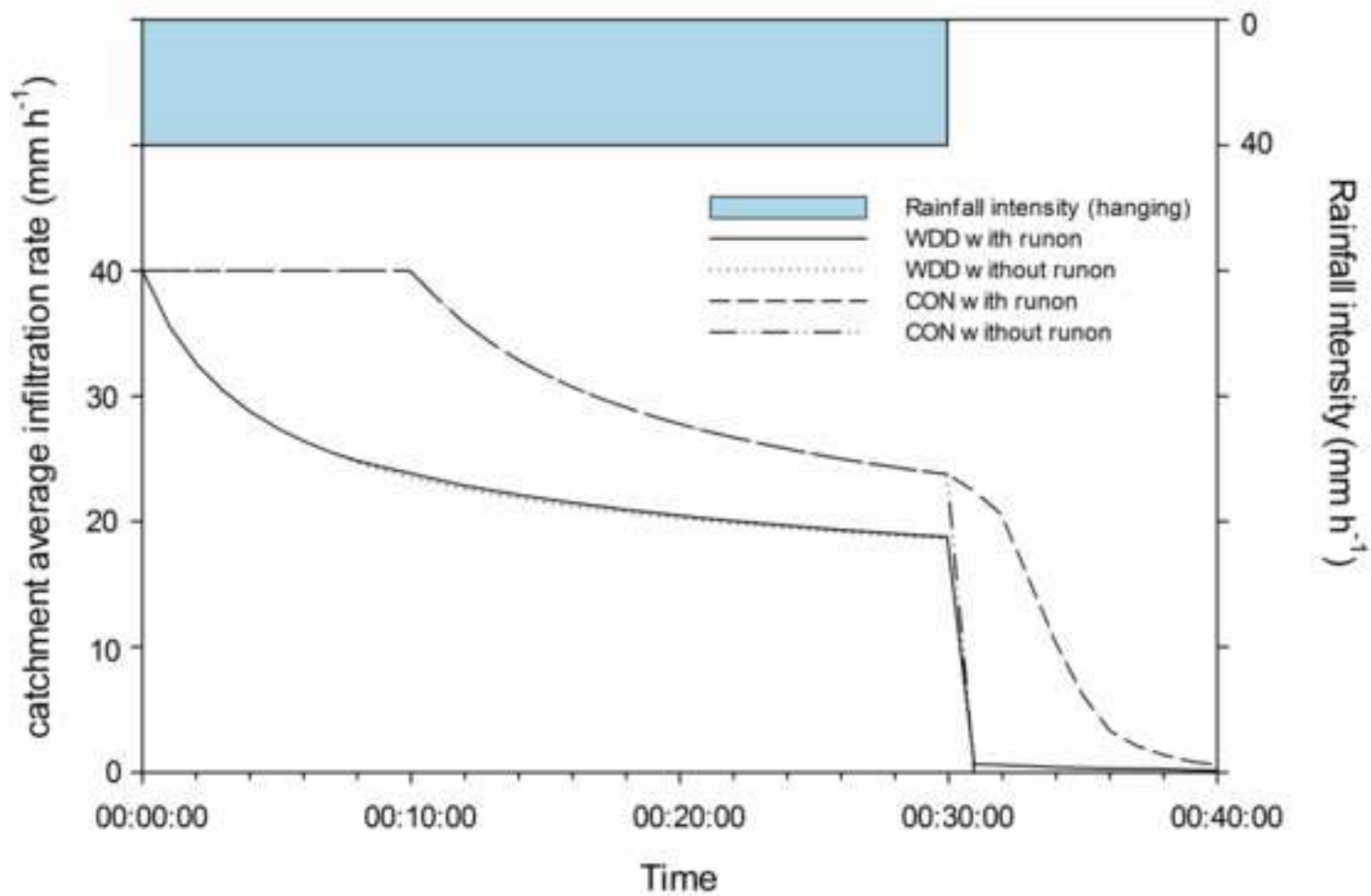
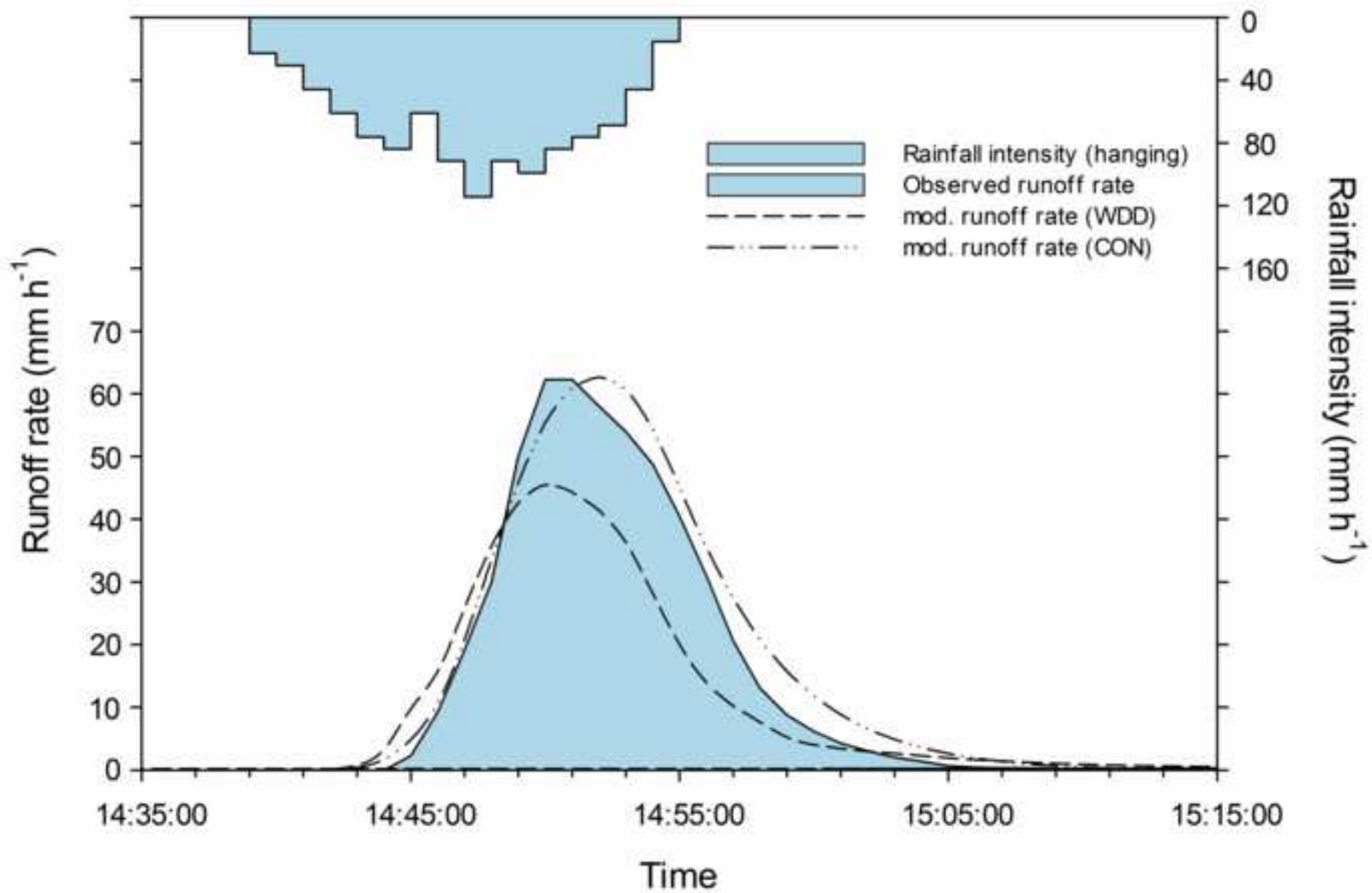
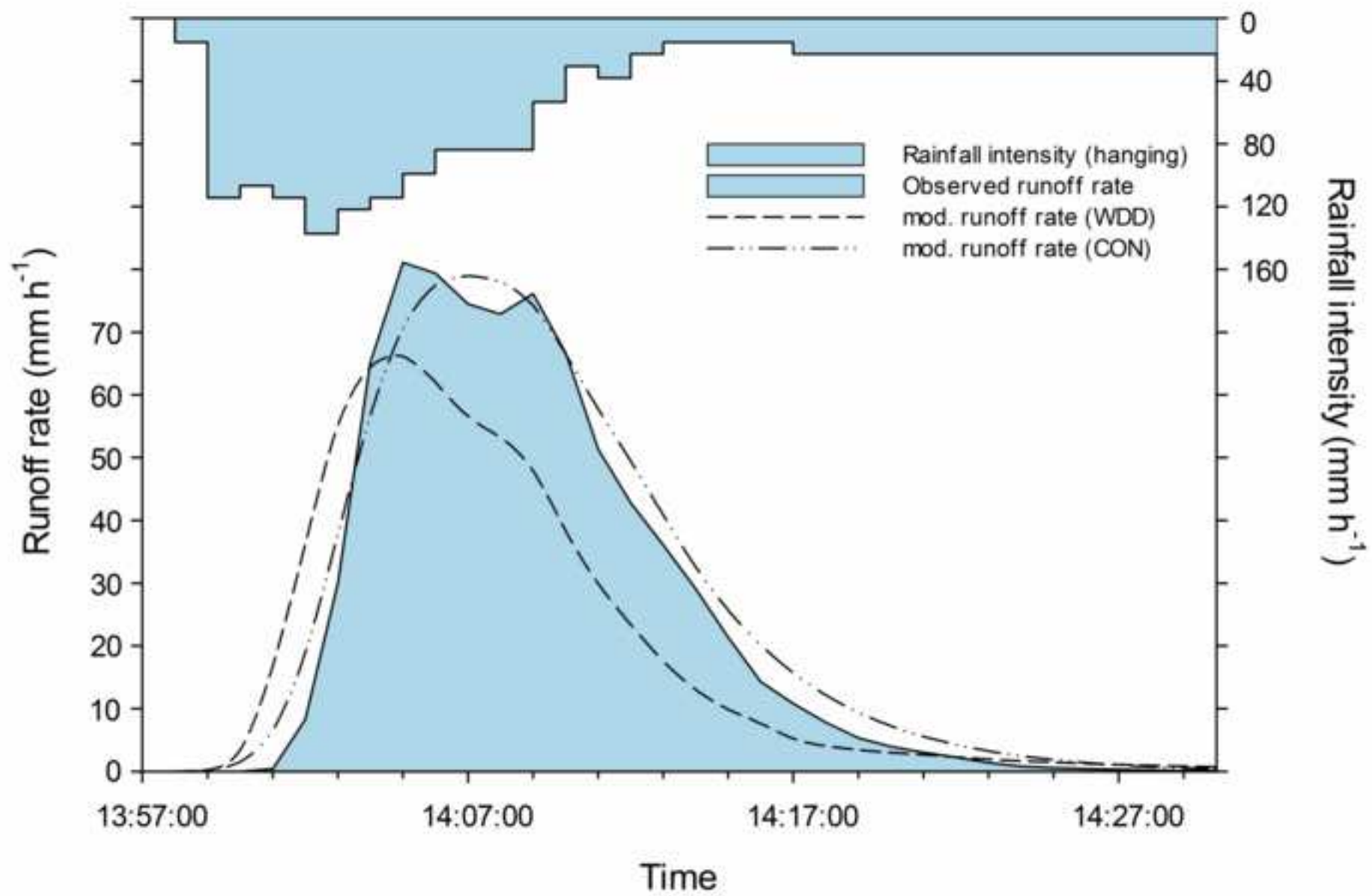
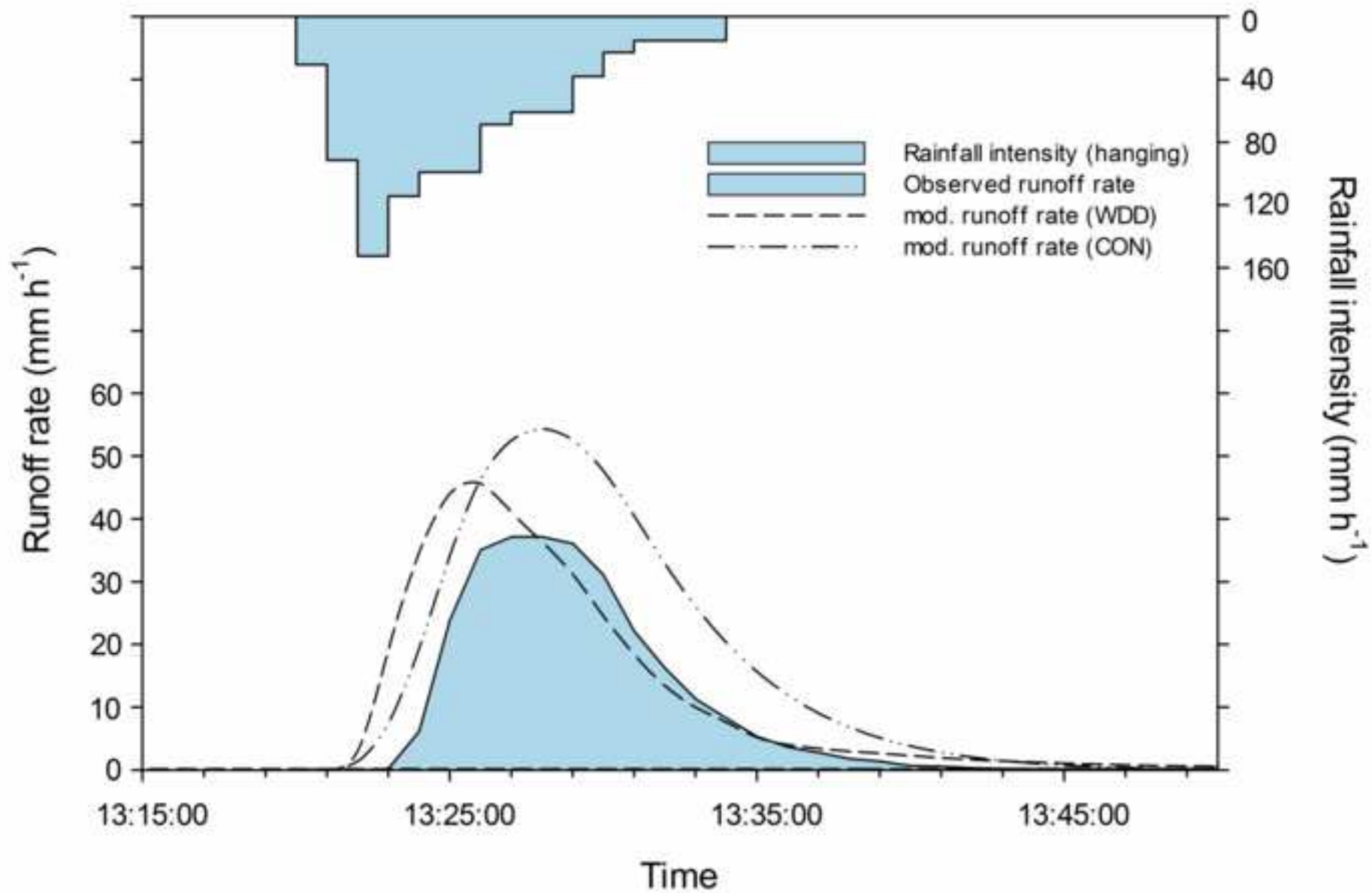


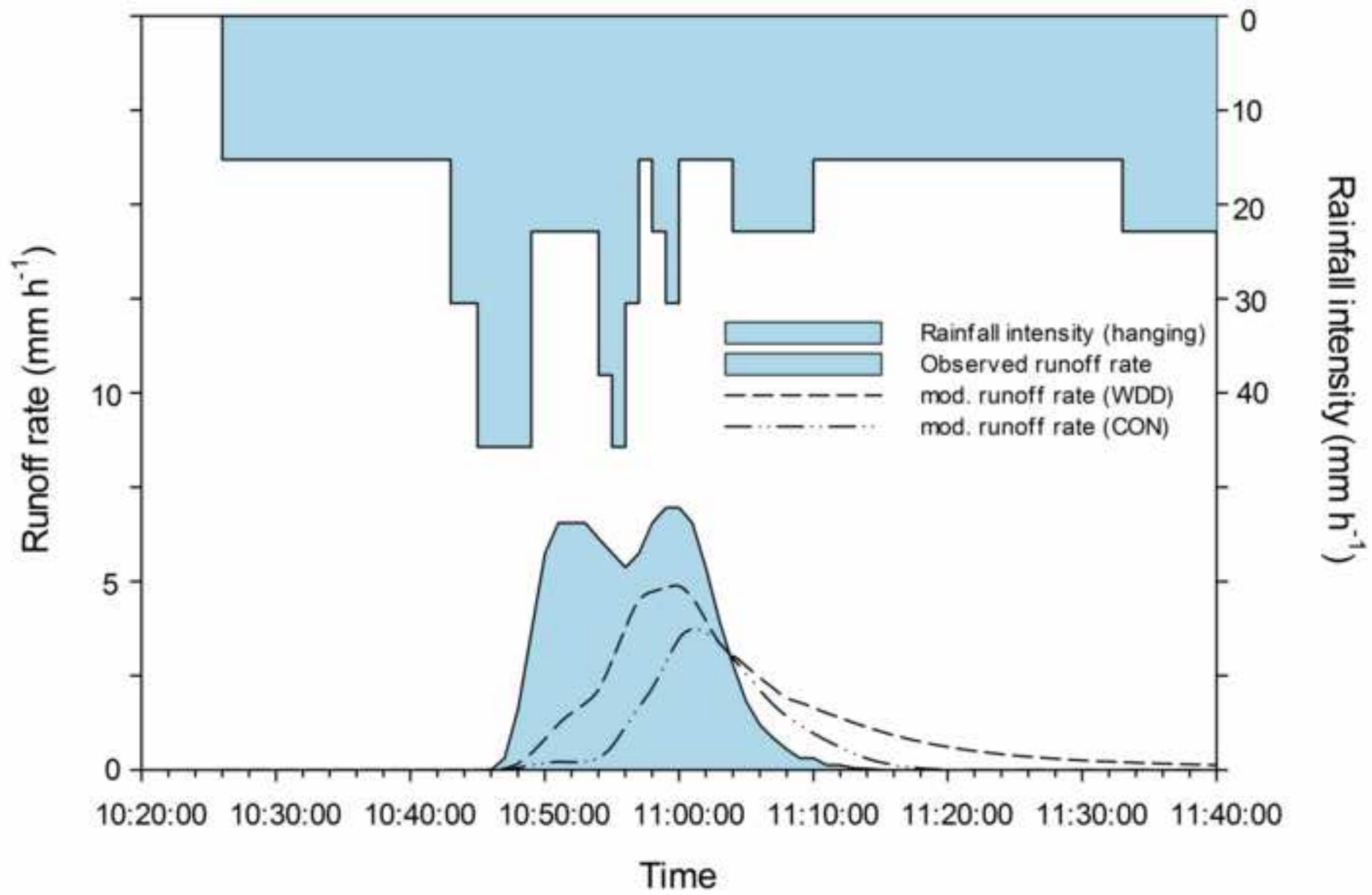
Figure 10

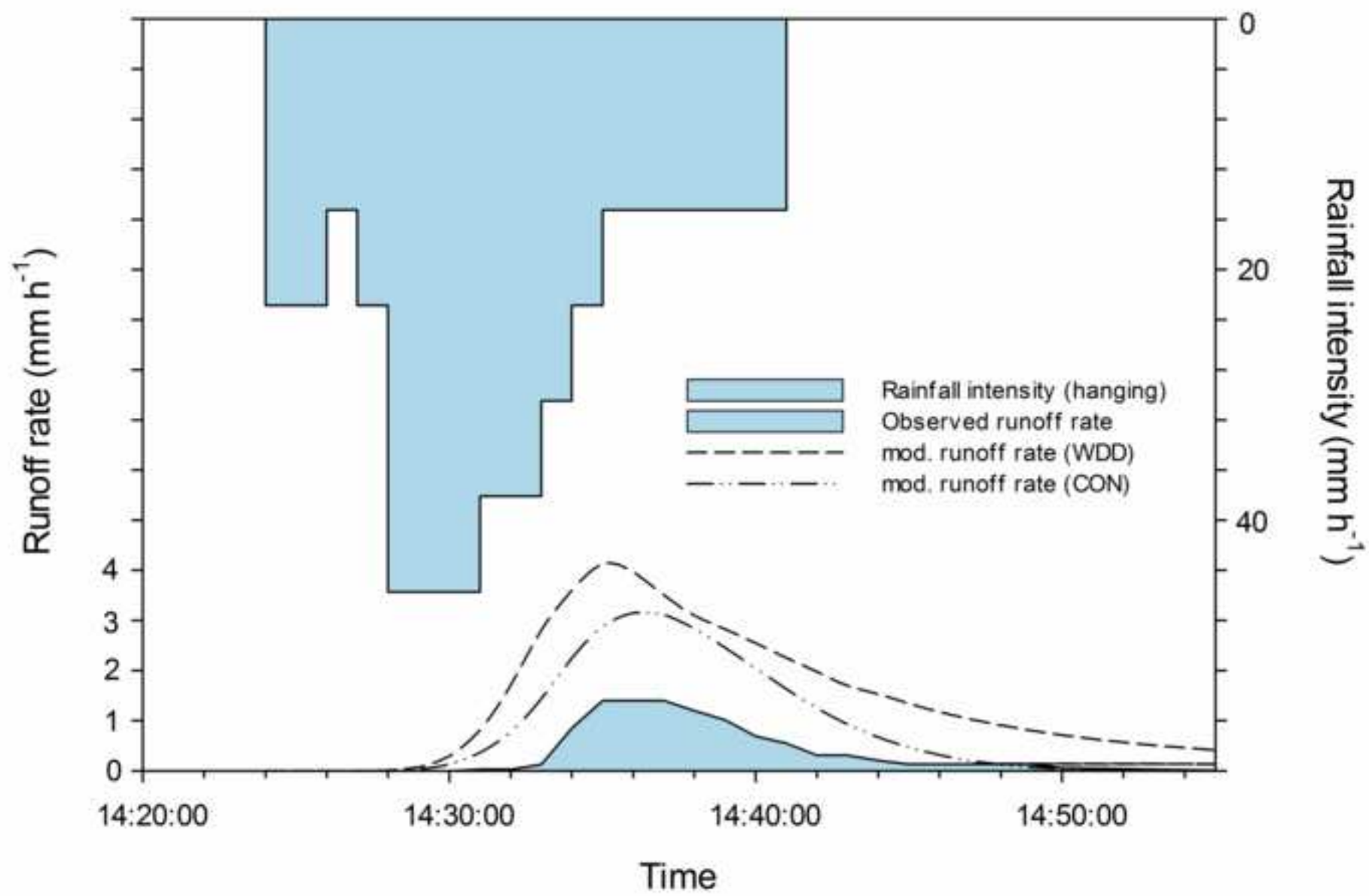












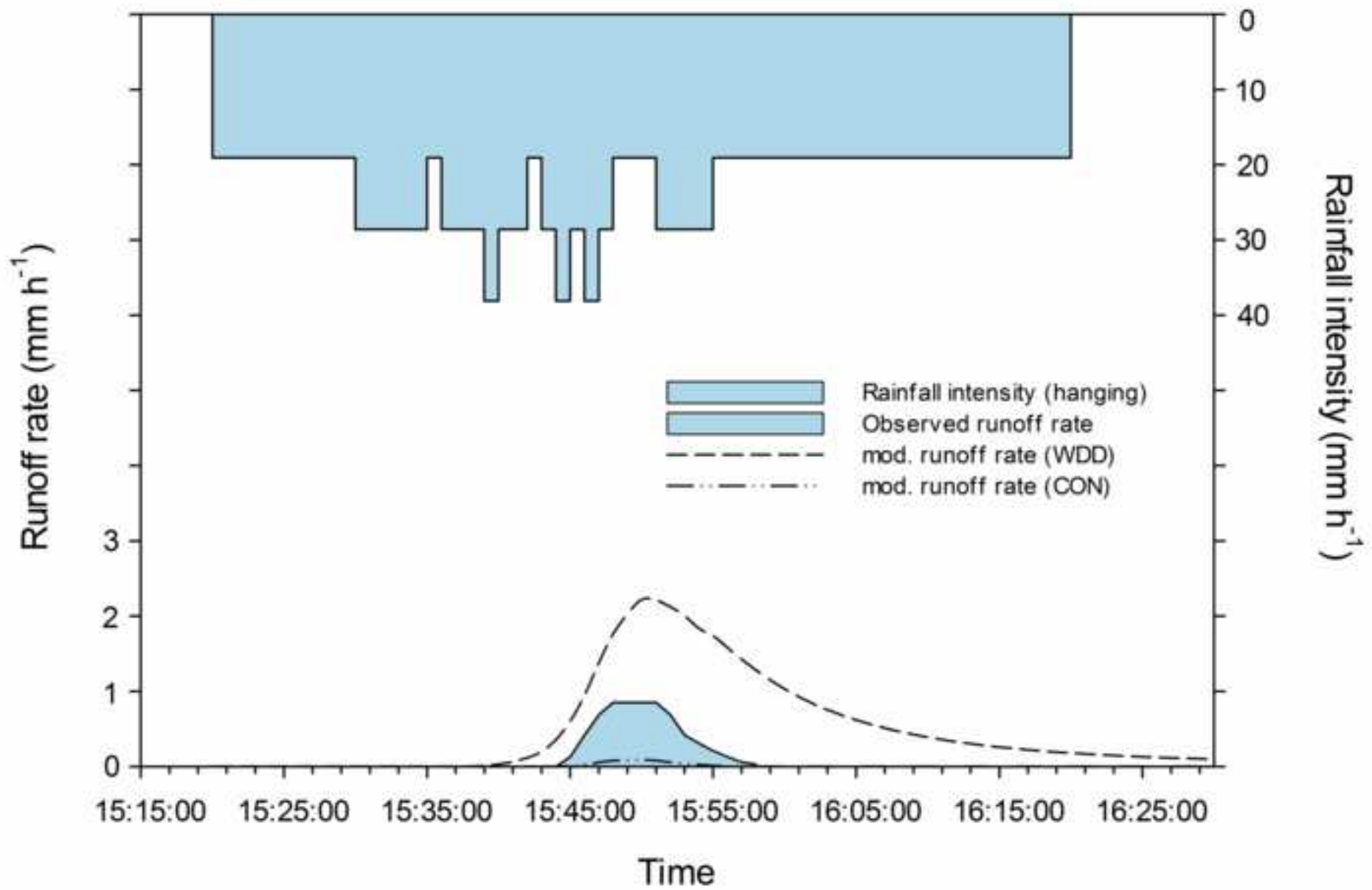


Table 1: Basic statistics of the rainfall simulation and rainfall events data set^a

	Rainfall simulations ^c			Rainfall events					
	Cal.	Val.	Val.	P	Q_i^d	Q_e^d	Q_p^d	Max. i	θ_i
	LP	LP	SP	(mm)	(m ³)	(mm h ⁻¹)	(mm h ⁻¹)	(mm h ⁻¹)	(-)
Number ^b	29 (5)	23 (4)	13 (3)	147	58	58	58	147	147
Mean	125.5	102.7	127.3	11.6	19.0	14.5	25.7	45.0	0.11
STDV	41.1	45.9	52.3	8.5	22.7	15.6	28.3	41.7	0.04
Min	61.5	25.4	46.7	4.6	0.4	0.51	0.69	1.9	0.03
Max	179.5	177.8	216.2	46.4	91.1	55.2	108.6	175.3	0.21

^aLP: large plots (6 x 2 m), SP: small plots (1.22 x 0.61 m); P : total precipitation of an event; Max i : maximum one minute interval rainfall intensity; θ_i : pre-storm (initial) volumetric water content of soil. ^b Value in brackets is number of plots. ^c Statistics refer to applied rainfall intensity (mm h⁻¹). ^d Q_i : total runoff, Q_e , effective discharge, Q_p : peak discharge; statistics apply to runoff producing events only.

Table 2: Optimized parameter values calibrated for the watershed scale from runoff hydrographs for both models (CON and WDD), with and without runoff infiltration, and parameters optimized for steady state rainfall simulation plot infiltration ('Plot')

	CON		WDD		Plot	
	With runoff infiltration	Without runoff infiltration	With runoff infiltration	Without runoff infiltration	CON	WDD
Ψ (mm)	31	22	139	175	-	-
μK (mm h ⁻¹)	-	-	16.5	14.5	-	62.4
K_e (mm h ⁻¹)	8	14	-	-	57.2	-
Manning's n	0.085	0.05	0.028	0.026	0.27	0.57

Table 3: Fraction of modelled events with a Nash-Sutcliffe Model Efficiency (ME) in a given class, coefficients of determination (R^2) for measured vs. modeled Q_b , Q_e and Q_p for all rainfall events, and objective measure (OBJ, Equation 21). Parameters were optimized to maximize OBJ, given the CAL dataset and validated with the VAL dataset (Table 1). Both models were calibrated with and without runoff infiltration.

		CON		CON		WDD		WDD	
		With runoff		Without runoff		With runoff		Without runoff	
		CAL	VAL	CAL	VAL	CAL	VAL	CAL	VAL
ME	> 0.75	0.37	0.11	0.37	0.21	0.37	0.32	0.37	0.29
	$0.75 > x > 0.5$	0.1	0.14	0.07	0.11	0.23	0.15	0.23	0.18
	$0.5 > x > 0$	0.13	0.21	0.16	0.18	0.07	0.07	0.07	0.07
	< 0	0.4	0.54	0.4	0.5	0.33	0.46	0.33	0.46
R^2	Q_t	0.82	0.62	0.88	0.76	0.94	0.86	0.94	0.85
	Q_p	0.91	0.67	0.94	0.69	0.89	0.72	0.89	0.72
	Q_e	0.93	0.78	0.94	0.74	0.93	0.79	0.93	0.79
OBJ		0.66	0.48	0.66	0.55	0.70	0.59	0.70	0.59

Highlights

- Development of new infiltration model based on Green and Ampt
- Combining water depth-dependent infiltration and partial contributing area concepts
- Good runoff predictions at rainfall simulator and small catchment scales
- Runon infiltration on hillslopes is an important process in semi-arid environments